Studies on liquid hydrocarbon synthesis using carbon oxides

炭素酸化物からの液体炭化水素の合成に関する研究

Jiaming Liang

梁嘉鳴

Supervisor: Prof. Noritatsu Tsubaki

Tsubaki Laboratory

Graduate School of Science and Engineering

University of Toyama

Preface

The combustion of fossil fuels for industrialization and transportation, which accompanies the rapid growth of cities, has resulted in the release of massive volumes of harmful gas into the atmosphere, such as CO_2 and CO. However, the excessive emissions of CO_2 will result in global warming, ocean acidification, and other environmental issues. Meanwhile, CO is also harmful to the human body. Therefore, the question of dealing with the CO_2 and CO emitted during industrial manufacturing has become an urgent concern. In this situation, and considering the targets of sustainable development, the conversion of CO_2 and CO into high-value chemicals has attracted increasing attention. In this manuscript, CO_2 and CO were converted into aromatics and C_5^+ chemicals via Fischer-Tropsch synthesis pathways, respectively, which is very meaningful for the environment and sustainable development.

Aromatics are chemicals prepared mostly from petroleum and coal tar, and can be used to synthesize industrial products. As crude oil becomes scarcer, there is an urgent need for a new method to produce aromatics. In chapter 1, CO_2 was converted into aromatics using composite catalysts containing a Fe-Zn bimetallic catalyst and a NaOH treated ZSM-5 zeolite.

A series of Fe–Zn catalysts promoted by potassium were successfully prepared by a co-precipitation and incipient wetness impregnation method. When the molar ratio of Fe to Zn was 3:1, the catalysts exhibited the highest performance and light olefin selectivity. Light olefins ($C_2^=$–$C_4^=$), as

important intermediates in the aromatization process, play an important role in aromatics selectivity. As a result, K-3Fe-Zn was used to combine with various H-ZSM-5 zeolites to construct bifunctional catalysts, where K-3Fe-Zn was responsible for the production of light olefin intermediates, while H-ZSM-5 zeolites were responsible for the aromatization of light olefins. The composite catalysts successfully realized the process from CO_2 to aromatics.

Furthermore, the different SiO_2/Al_2O_3 ratios of ZSM-5 zeolites, the concentrations of NaOH solution, and the weight ratios of K-3Fe-Zn to ZSM-5 zeolite were also systematically investigated in detail. We found that when the SiO_2/Al_2O_3 ratio was 21, the concentration of NaOH was 0.2 M, and the weight ratio was 1:3, the composite catalysts showed the highest aromatic selectivity, which indicated the highest light olefin transport and conversion efficiency.

Combined with experimental data and theoretical analysis, the alkenes produced from K-Fe/Zn could be effectively converted into aromatics via in situ dehydrogenation and cyclization on the acidic sites of H-ZSM-5. The bifunctional catalyst presented the highest aromatics selectivity of 45.2%, with a CO_2 conversion of 42.6%.

In chapter 2, we successfully produced C_5^+ chemicals via a nitrogen-regulated-graphene supported Fe nanoparticle catalyst synthesized by the quick microwave method. Long-chain hydrocarbons (C_5^+), as carbon-neutral fuels, have high energy density and facile mobile storage capacity, and have attracted wide attention. However, owing to the inertia of CO_2 molecules and imprecise control of carbon chain propagation during CO_2 hydrogenation, efficient catalytic

conversion of CO_2 into long-chain hydrocarbons remains a huge challenge. Meanwhile, the long calcination time during the traditional catalyst preparation process greatly increases the cost and difficulty of preparation.

Based on these difficulties, we reported a facile *in situ* engineering method for making N-doped graphene-supported iron NPs. This was accomplished using a microwave treatment with a solid precursor under the protection of nitrogen atmosphere. It was worth noting that the catalyst was not processed by traditional heating equipment (for example, calcination) during the preparation process and the preparation cycle was rather shorter than conventional processes. With the incorporation of N atoms, catalytic activity was obviously enhanced and the conversion was as high as 97% (15%Fe/AG(12 h) -W(10)), which was higher than conventional catalyst systems. Meanwhile, 40.0% C_5^+ selectivity was obtained. N-doped graphene supported iron NPs assisted by microwave treatment open a promising route for the development of advanced FTS catalysts.

This design of graphene supported iron nanoparticles with the utilization of rapid heating treatment provides a new strategy for FTS to produce high value-added products (heavy hydrocarbons), and sheds a light on the rational design of high efficiently catalysts for practical industry in the future.

In conclusion, the two kind of catalysts (K-3Fe-Zn & ZSM-5 composite catalysts and Fe/AG-W catalysts) achieved the conversion of CO_2 to aromatics and CO to C_5^+ hydrocarbons, respectively, which is meaningful for the nowadays environment and sustainable development. The development of

high efficiency catalysts provided a new view in identifying the active sites and the pathways to the target products for Fischer-Tropsch synthesis.

Contents

Contents

Chapter 1

Direct conversion of CO_2 to aromatics over K-Zn-Fe/ZSM-5 catalysts via a Fischer-Tropsch synthesis pathway

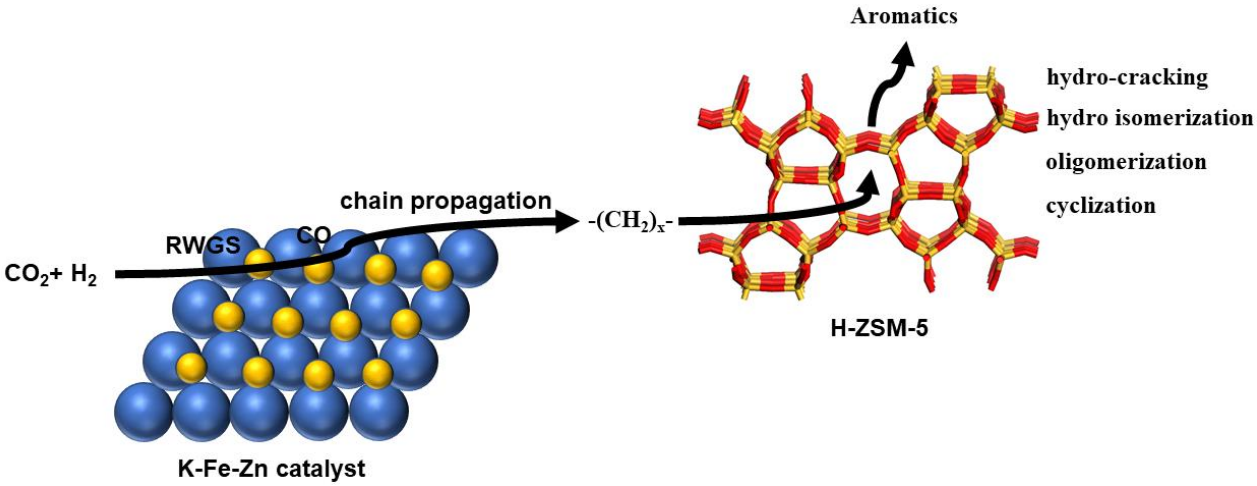

Abstract

A series of Fe–Zn catalysts promoted by potassium were successfully prepared by a co-precipitation and incipient wetness impregnation method. The obtained K-Fe/Zn catalysts exhibited excellent performance for CO_2 hydrogenation toward C_2–C_4 olefin formation with high selectivity. A series of efficient bifunctional K-Zn-Fe/ZSM-5 catalysts for CO_2 hydrogenation were constructed by combining the K-Fe/Zn catalysts with H-ZSM-5 with different SiO_2/Al_2O_3 ratios, which exhibited a superior aromatics selectivity especially when utilizing a zeolite with NaOH solution pretreatment. Meanwhile, the relationships between catalytic performance and the microenvironment of zeolite were systematically studied. Furthermore, the correlation between aromatic selectivity and H-ZSM-5 weight was also investigated in detail. Combined with experimental data and theoretical analysis, the alkenes produced from K-Fe/Zn could be effectively converted into aromatics via in situ dehydrogenation and cyclization on the acidic sites of H-ZSM-5. The bifunctional catalyst presented the highest aromatics selectivity of 45.2%, with a CO_2 conversion of 42.6%.

Keywords:

CO_2 hydrogenation; Fischer-Tropsch synthesis; Aromatic synthesis; K-Fe/Zn catalysts; Light olefins

1. Introduction

Human activities such as industrial and agricultural output, automobile emissions, and deforestation generate a substantial amount of CO_2, which contributes to global warming, ocean acidification, and other catastrophic repercussions [1, 2]. As a result, different groups are paying more attention to the conversion of CO_2 into high-value compounds [3], which is regarded as a promising strategy for long-term sustainable development [4]. CO_2 is an appropriate raw material for organic synthesis from the standpoint of environmental conservation because it is an inexpensive and abundant carbon source [5]. CO_2 hydrogenation to form basic chemicals such as methanol and hydrocarbons has attracted considerable attention in the past decades. However the inertness of CO_2 and the energetic hurdles associated with carbon-carbon bonds have always made direct synthesis of heavy hydrocarbons from CO_2 hydrogenation difficult [6–10].

Benzene is a chemical prepared mostly from petroleum and coal tar, and can be used to produce industrial chemicals [5, 11, 12]. As crude oil becomes scarcer, there is an urgent need for a new method to produce benzene [13–14]. The direct synthesis of aromatics from CO_2 with methanol as an intermediate has been achieved in recent years: the catalysts during the reaction can simultaneously complete the processes of methanol synthesized from CO_2 at high temperatures and methanol conversion to aromatics [15–17]. Due to the high selectivity of the byproduct CO which could be formed from reverse water gas shift (RWGS, $CO_2 + H_2 \rightarrow CO + H_2O$) reaction, only a tiny quantity of the target aromatics are produced under specific reaction conditions, making this route inefficient.

Recently, Wang et al. reported the direct synthesis of aromatics from CO_2 via the methanol route using a hybrid Cr_2O_3/H-ZSM-5 catalyst [18]. A CO_2 conversion of 34.5% and an aromatic selectivity of 76.0% were attained. However, it is difficult to satisfy the demand for industrial applications in terms of low space time yield (STY) (Table 1.1). More recently, bifunctional catalysts by coupling Fischer-Tropsch synthesis (FTS) catalysts and zeolite catalysts achieved a promising results. Wang et al. used a modified FTS method to achieve a high aromatic yield (203.8 g kg_{cat}^{-1} h^{-1}) [17]. This finding presented a significant increase in the generation of aromatic hydrocarbons.

Iron-based catalysts are ideal options for CO_2 conversion via a modified FTS due to its catalytic capacity in both the RWGS and FTS reactions [19, 20]. Under working reaction conditions, Fe-based catalysts contain two parts of active sites: Fe_3O_4 for CO intermediate production and Fe_5C_2 for subsequent chain propagation [21]. The effectiveness of iron catalysts can be enhanced by adding alkali metal elements such as K and Na. The favorable carburization, increased CO_2/H_2 adsorption, and poor secondary hydrogenation ability are attributed to the promotional effects [22]. Kosol et al. constructed a nitrogen-functionalized carbon supported iron catalyst for CO_2 hydrogenation, and found that the heavy hydrocarbon selectivity (C_5^+) could increase from 14.8% to 39.8% with the addition of the alkaline K promoter [22]. Previously, Zn promoter was applied to accelerate the FTS reaction and improve the catalyst stability as well as light olefins selectivity, apart from adjusting reaction molecules adsorption and dissociation properties [23]. For instance, Zhang et al. enhanced selectivity toward light olefins by incorporating Zn promoter in the iron catalyst for CO_2 hydrogenation. When Zn was added

to an iron matrix, it could exist in the form of $ZnFe_2O_4$ spinel phase and the ZnO phase, which could increase the surface area, improve the Fe-Zn interaction, change the reduction, and CO_2 adsorption behaviors. The selectivity of C_2–C_4 olefins among total hydrocarbons could reach 53.58%, as well as the ratio of olefins to paraffins in the C_2–C_4 fraction reached 6.86 with a CO_2 conversion of 51.03% [23].

H-ZSM-5 zeolites with suitable pore shapes have been employed as ideal catalysts for aromatics formation from methanol or alkenes [16, 17, 24, 25]. Hydrocracking, hydroisomerization, oligomerization, cyclization, and H transfer over an acidic H-ZSM-5 zeolite would transform the produced olefins into aromatics or isoparaffins as the FTS process occurs [26]. However, due to the presence of micropores, the catalytic efficiency of typical ZSM-5 zeolite-supported catalysts might be restricted in some situations. Micropores can cause poor diffusivity of hydrocarbon molecules, which has a detrimental influence on the reaction rate [27, 28]. To address this issue, several alternative techniques have been tried. One technique involves insertion of mesopores into each zeolite crystal individually. This strategy was generally accomplished by appropriate post-treatments such as dealumination or desilication, which caused the zeolite crystals to partially disintegrate [29]. Groen et al. investigated the formation of mesopores in H-ZSM-5 as a result of selective desilication with NaOH, successfully producing two hierarchical pore systems [30–32]. Bjrgen et al. also observed that NaOH treatment improved the catalytic performance in the MTG process [33, 34]. Obviously, constructing a hierarchical structure will improve the mass-transfer efficiency of intermediates during catalysis

processes. Furthermore, the hollow structures in H-ZSM-5 can effectively enhance the selectivity of aromatics by shortening the diffusion pathway of the $–(CH_2)_x–$ intermediates. The generated aromatics are simpler to expel from hollow H-ZSM-5 without the undesired overhydrocracking reaction that occurs in the three-dimensional channels of untreated ZSM-5 [17].

Obviously, aromatics selectivity and distribution are largely influenced by the properties of catalysts such as the zeolites and the type of Fe-based catalyst [27, 34]. In this report, a series of Fe–Zn catalysts promoted by K were successfully prepared by a co-precipitation and the incipient wetness impregnation method. The obtained K-Fe/Zn catalysts exhibited excellent activity for CO_2 hydrogenation as well as high C_2–C_4 olefins selectivity. Based on this consideration, a series of bifunctional catalysts containing K-nFe/Zn and ZSM-5 catalysts were designed for CO_2 hydrogenation to aromatics. To further improve aromatic selectivity, H-ZSM-5 zeolites were treated by NaOH solution, meanwhile different weights of H-ZSM-5 zeolites after NaOH treatment were combined with K-3Fe-Zn which presented the best light olefins selectivity. In the reaction, the alkenes produced from K-3Fe/Zn catalyst could be effectively converted into aromatics via in situ dehydrogenation and cyclization on the acidic sites of H-ZSM-5. The aromatic selectivity in the hydrocarbons reached 45.2% with a CO_2 conversion of 42.6%.

Table 1.1 Comparison of the yield and selectivity of aromatics of past works

catalyst	T(℃)	P(MPa)	CO_2 Conv. (%)	CO Sel. (%)	Aromatics Sel. (%)	STY of A ($g_{CH2}·kg_{oxide}^{-1}·h^{-1}$)
Fischer-Tropsch pathway						
FeK1.5/HSG/H-ZSM-5	340	2	35.0	39.0	68.0	1132.4
Na-Fe@C/H-ZSM-5	320	3	33.3	13.3	50.2	203.8
NaFe/H-ZSM-5	320	3	27.7	16.0	44.5	163.5
This work	320	3	44.2	10.1	35.1	176.2
Methanol-intermediate pathway						
$ZnO-ZrO_2$/H-ZSM-5	320	4	14.1	44.0	73.0	20.8
Cr_2O_3/H-ZSM-5	350	3	16.4	38.2	67.9	20.5

2. Experimental section

2.1 Catalyst preparation

nFe/Zn (n=6, 3, 1, 0) catalysts were prepared by using $Fe(NO_3)_3·9H_2O$ [Wako Pure Chemical Co.] and $Zn(NO_3)_2·6H_2O$ [Wako Pure Chemical Co.] as Fe and Zn sources, respectively. Na_2CO_3 [Sigma-Aldrich Co.] was the precipitator. Complexes with Fe/Zn molar ratios of 1:0 (20.2 g, 0 g), 6:1 (17.3 g, 2.12 g), 3:1 (15.2 g, 3.72 g) and 1:1 (10.1 g, 7.4 g) were dissolved in 100 mL deionized water with stirring, and 10.6 g Na_2CO_3 was dissolved in 200 mL deionized water simultaneously. The two aforementioned solutions were added dropwise to deionized water with stirring and maintained at a pH of approximately 8. The co-precipitation was completed and aged at 60 °C for 1 hour. The catalysts were then washed and filtered until the pH was 7 and then dried at 60 °C in an oven overnight before

being calcined at 400°C for 3 hours. The 1 wt% K-nFe/Zn catalysts were prepared by impregnating nFe/Zn with a K_2CO_3 solution. The as-prepared K-nFe/Zn catalysts were denoted as K-Fe, K-6Fe/Zn, K-3Fe/Zn, and K-1Fe/Zn, respectively. Thereinto, the numbers of 6, 3, and 1 represented Fe/Zn molar ratios. K-3Fe/Zn was further combined with H-ZSM-5 zeolite with varied SiO_2/Al_2O_3 ratio as 130, 85, 46 or 21 by physical mixing. Both K-3Fe/Zn and H-ZSM-5 had a diameter of 500 μm.

NaOH solution of 0.1 M, 0.2 M, 0.4 M, or 0.6 M was selected to treat commercial zeolite. For instance, parent zeolites were added to the above solutions, and treated at 80 °C for 1 h. After that, the obtained sample was filtered and washed three times, and then calcined at 550 °C for 5 h. NH_4NO_3 solution (200 mL, 1.0 mol L^{-1}) was used to remove residual Na^+ ions by ion exchange and successive calcination. The resulting zeolites were denoted as H-ZSM-5-X, in which X indicated the NaOH concentration.

2.2 Catalyst characterization

X-ray diffractometer (Rigaku RINT 2400) with Cu Kα radiation was used to obtain diffraction patterns. The surface morphologies of the catalysts were investigated using scanning electron microscopy (SEM, JEOL JSM-IT700HR). Transmission electron microscopy (TEM, JEOL JEM-2100F) was used to observe particle sizes and distribution at an acceleration voltage of 100 kV. The surface areas of the catalysts were determined using N_2 adsorption-desorption experiments at –196 °C (QUANTA AUTOSORB-1). The catalysts were degassed for 8 hours at 200 °C under vacuum

conditions prior to the measurements. The element contents in the catalysts were measured by a Phillips 2400 X-ray fluorescence (XRF) spectrometer.

A BELCAT-II-T-SP analyzer with a thermal conductivity detector (TCD) was used to acquire H_2 temperature-programmed reduction (H_2-TPR) profiles. 50 mg sample was firstly pretreated with He for 1 hour at 300 °C. When the temperature was lowered to 50 °C, 5 vol% H_2/Ar gas mixture was supplied to the reactor (30 mL/min). Finally, H_2-TPR profiles were obtained at temperature ranging from 50 to 900 °C, with a heating rate of 10 °C/min. The same equipment was also used to investigate the CO_2 or NH_3 temperature-programmed desorption (TPD). 50-mg sample was reduced for 2 hours at 400 °C under a 100% H_2 gas flow (30 mL/min). The temperature of the catalysts was reduced to 50 °C under a He gas flow (30 mL/min) after reduction. The reactor was subsequently filled with a 100% CO_2 or 5% NH_3/He gas mixture for 1 hour. He was then inserted into the reactor to remove the physically-adsorbed CO_2 or NH_3. The CO_2-TPD and NH_3-TPD profiles were recorded from 50 to 900 °C with a heating rate of 10 °C/min. A Thermo Fischer Scientific ESCALAB 250 Xi instrument with a catalyst pretreatment chamber for altering the gas composition was used to conduct the X-ray photoelectron spectroscopy (XPS) analysis.

2.3 Catalytic tests

The catalytic performance of the catalyst was evaluated in a fixed-bed reactor with an internal diameter of 6 mm. The catalyst was reduced by pure H_2 at 400 °C for 8 h before the reaction. After

reduction, the temperature was dropped to 270 °C. Subsequently, $CO_2/H_2/Ar$ (27.0 vol% / 68.0 vol% / 5.0 vol%) reactant gas was introduced into the reactor, and the system was pressured gradually to 3.0 MPa and increased to 320 °C. To collect the heavy hydrocarbons and eliminate the water generated by the reaction, an ice trap was placed between the reactor and the back pressure valve. An off-line gas chromatograph (GC, Shimadzu GC-2014) equipped with a flame ionization detector (FID) and a DB-1 capillary column was used to examine the heavy hydrocarbons. To identify the gas-phase products, two online gas chromatography systems (GL sciences GC320 and GC390B) were used: one with a thermal conductive detector (TCD, GC320) and an active charcoal column for Ar, CO, CH_4, and CO_2 analysis; and another with an FID (GC390B) and a GS-ALUMINA PT column for light hydrocarbon analysis. An FID (GC-2025) and a DB-WAX column were used to identify meta-xylene and para-xylene.

Eqs. 1, 2, and 3 were used to compute the CO_2 conversion, CO selectivity, and hydrocarbon selectivity, respectively [35].

CO_2 conversion (%) = $(CO_{2\text{-in}} - CO_{2\text{-out}})/CO_{2\text{-in}} \times 100\%$ (1)

The mole fraction of CO_2 in the intake is $CO_{2\text{-in}}$, while the mole fraction of CO_2 in the exit is $CO_{2\text{-out}}$.

CO selectivity (%) = $CO_{out}/(CO_{2\text{-in}}\text{-}CO_{2\text{-out}}) \times 100\%$ (2)

Where CO_{out} represents the mole fraction of CO in the outlet.

C_i hydrocarbon selectivity (C-mol%)=

(moles of C_i hydrocarbons $\times$ i)/($\sum_{i=1}^{n}$ moles of Ci hydrocarbons $\times$ i) $\times$ 100% (3)

The mass balances were calculated as following: carbon-mol from total products / carbon-mol from CO_2 converted × 100%. And all the results were above 90%.

3. Results and discussion

3.1 Phase composition of K-nFe/Zn catalysts

Powder XRD measurements were used to identify the phase composition of the K-nFe/Zn catalysts (Fig. 1.1). Fig. 1.1a showed the XRD patterns of fresh catalysts. In terms of K-Fe catalyst, characteristic diffraction peaks ascribed to Fe_2O_3 (PDF#33-0664) were observed. With increasing Zn content, diffraction peaks of magnetite (Fe_3O_4, PDF#19-0629) and maghenite-C (Fe_2O_3, PDF#39-1346) were observed for the K-3Fe/Zn and K-6Fe/Zn catalysts, respectively. As the Zn content increased further, diffraction peaks at 2ɵ= 31.8°, 36.3°, and 47.5° were observed in the K-1Fe/Zn catalyst, corresponding to zincite (ZnO, PDF#36-1451). The absence of Zn diffraction peaks at lower Zn contents (K-Fe, K-6Fe/Zn, K-3Fe/Zn) could be attributed to the good dispersion of Zn. Similarly, no diffraction peaks corresponding to K species were observed owing to the low content and benign dispersion.

The crystallite sizes of iron oxides in the four catalysts were calculated by the Scherrer equation, as shown in Table 1.2. The particle sizes of these catalysts were between 12 and 19 nm. Upon addition of Zn, the sizes of the iron oxide in the K-1Fe/Zn, K-3Fe/Zn and K-6Fe/Zn catalysts were smaller than

that in K-Fe catalyst, in which K-3Fe/Zn presented smallest size of iron species. This was consistent with the specific area and pore parameter results presented in Table 1.3. As seen in Table 1.3, upon the gradual addition of Zn, the specific surface area of the K-nFe/Zn catalysts gradually increased and reached a maximum when Fe/Zn was 3. Previous studies showed that the addition of Zn can enhance the dispersion of the iron phase and expand the specific surface area [36, 37]. As a consequence, K-nFe/Zn exhibited a high surface area than K-Fe catalyst. However, the addition of excessive Zn led to the formation of large ZnO clusters, resulting in a decrease in the specific surface area.

Table 1.2 Crystallite sizes of iron oxides calculated by Scherrer equation.

Catalysts	Phase of iron oxide	Crystallite of iron oxide (nm)
K-Fe/Zn	Fe_3O_4	14.7328
K-3Fe/Zn	Fe_3O_4	12.9060
K-6Fe/Zn	Fe_2O_3	14.0682
K-Fe	Fe_2O_3	19.4400

Table 1.3 Specific area and pore parameters results of the K-nFe/Zn catalysts.

Catalysts	S_{BET} (m^2/g)	Pore diameter (nm)	Pore volume (cm^3/g)
K-Fe/Zn	62.56	6.23	0.18
K-3Fe/Zn	79.94	4.21	0.24
K-6Fe/Zn	65.27	7.75	0.19
K-Fe	43.91	8.52	0.15

The XRD diffraction peaks of spent catalysts were shown in Fig. 1.1b. The characteristic diffraction peaks of carbide (Fe_5C_2, PDF#20-0508) were observed for all the four spent catalysts. With

the addition of Zn, the diffraction peaks of Fe_3O_4 (PDF#19-0629) were observed in the spectra of spent K-6Fe/Zn and K-1Fe/Zn, respectively. While there were no Fe_3O_4 diffraction peaks observed in spent K-3Fe/Zn spectra, which was due to its well reduction ability. As the Zn content increased, diffraction peaks of ZnO appeared and increased in intensity in the spectra of the spent K-6Fe/Zn, K-3Fe/Zn and K-1Fe/Zn.

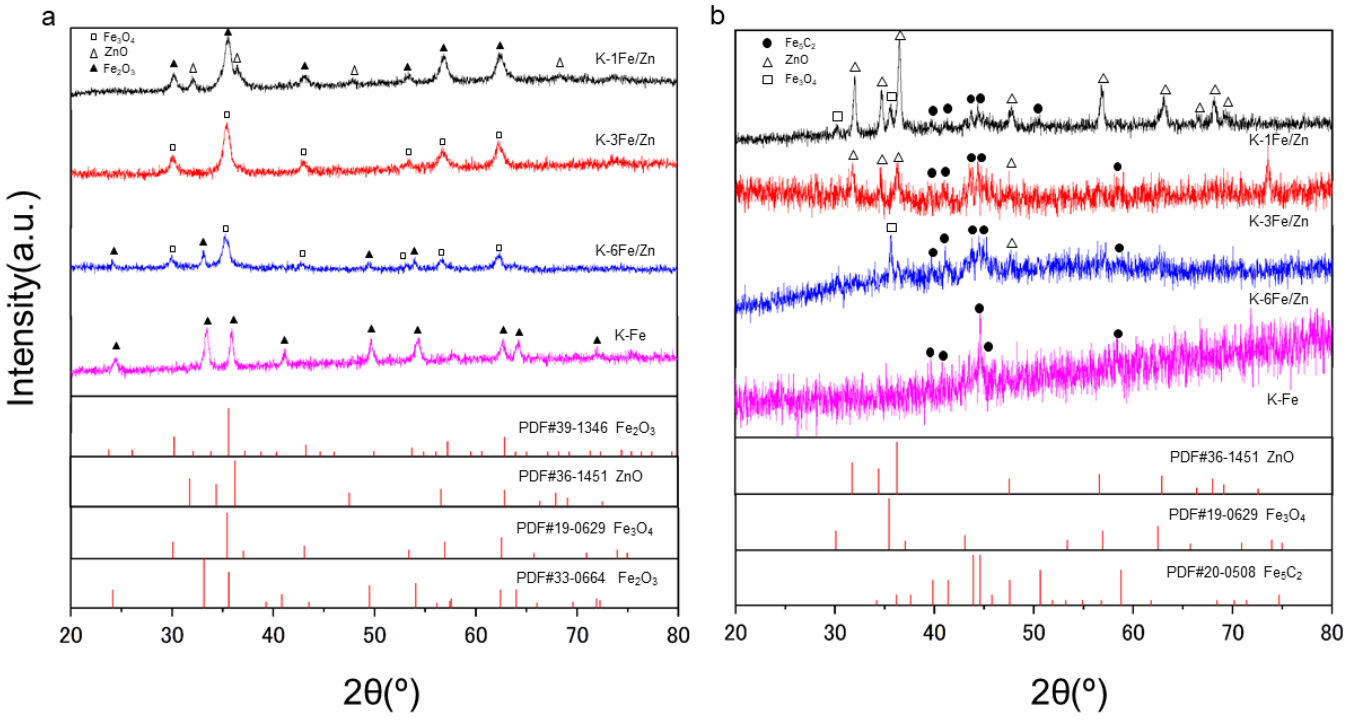

Fig. 1.1 XRD patterns of fresh K-nFe/Zn (a) and spent K-nFe/Zn (b).

3.2 Morphologies and particle size distribution of different catalysts

SEM images of K-nFe/Zn catalysts were depicted in Fig. 1.2. The morphologies and structures of different catalysts were irregular. As presented in Fig. 1.2a–c, with the increase of Zn, the sizes of K-

nFe/Zn catalysts became smaller, which was also demonstrated in Fig. 1.1 and Table 1.2.

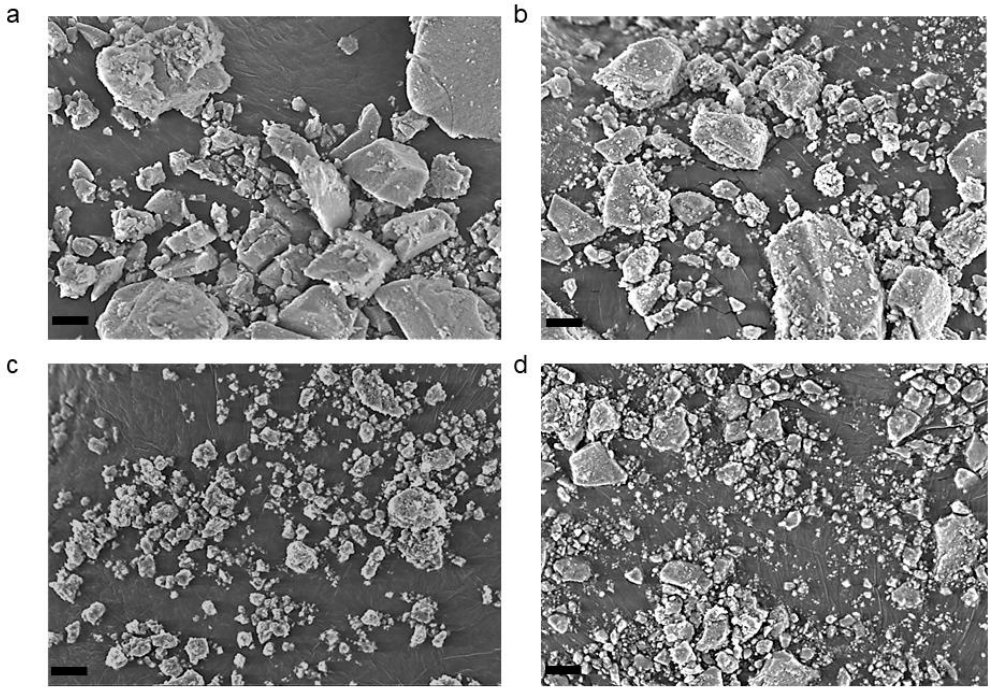

Fig. 1.2 SEM images of K-Fe (a), K-6Fe/Zn (b), K-3Fe/Zn (c), K-1Fe/Zn (d); the bars stand for 10 μm.

TEM and high-resolution TEM (HR-TEM) images of fresh K-3Fe/Zn with calculated particle sizes were shown in Fig. 1.3. As seen, the particle sizes of these samples ranged from 5 nm to 20 nm, as depicted in Fig. 1.3b. The average particle size was 12.4 nm, which were generally consistent with the particle size obtained by the Scherrer equation in the XRD results (Table 1.2). Fig. 1.3d showed the HR-TEM image of the fresh K-3Fe/Zn catalyst. The lattice spacing was 0.25 nm, which was corresponded to the Fe_3O_4 (311) plane spacing and were consistent with the Fe_3O_4 in Fig. 1.1. HR-TEM images of spent K-nFe/Zn catalysts were displayed in Fig. 1.4 to validate the presence of iron carbides. The lattice spacing values were 0.22 nm, which were related to the lattice spacings of (101)

planes in Fe_5C_2 species. Carbides as an active phase played a crucial role for chain propagation processes.

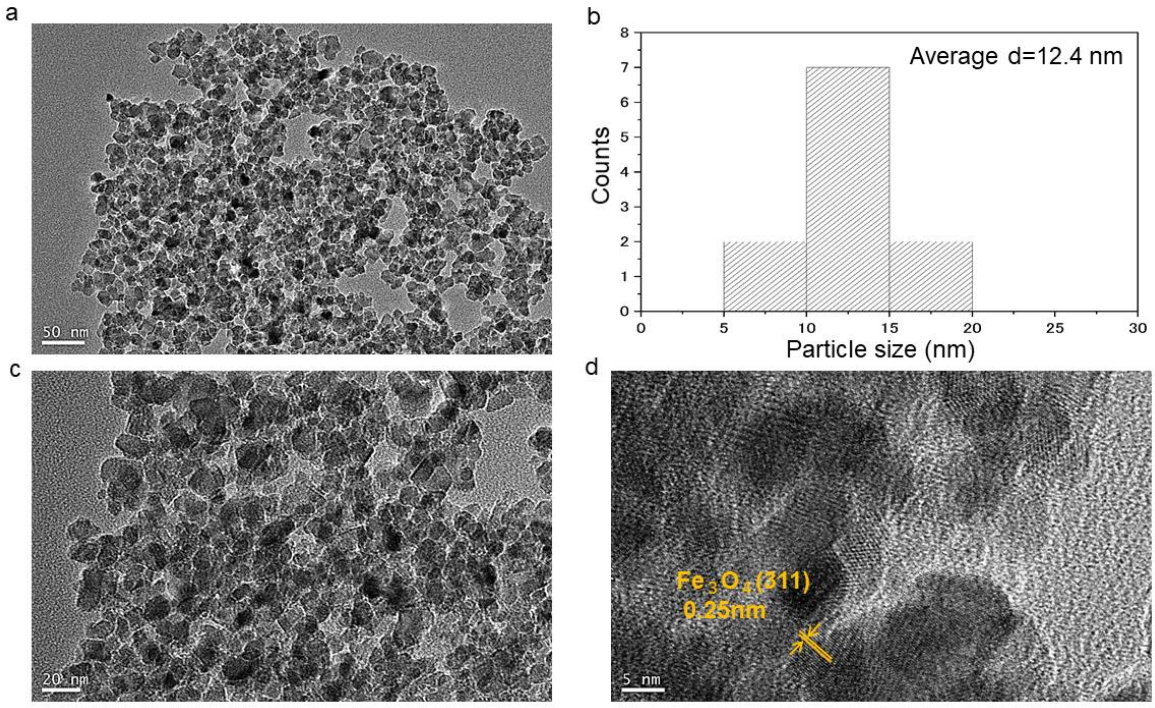

Fig. 1.3 TEM images of fresh K-3Fe/Zn (a) (c) and particle size distribution of fresh K-3Fe/Zn (b) and HR-TEM image of fresh K-3Fe/Zn (d). The bars stand for 50 nm, 20 nm and 5 nm.

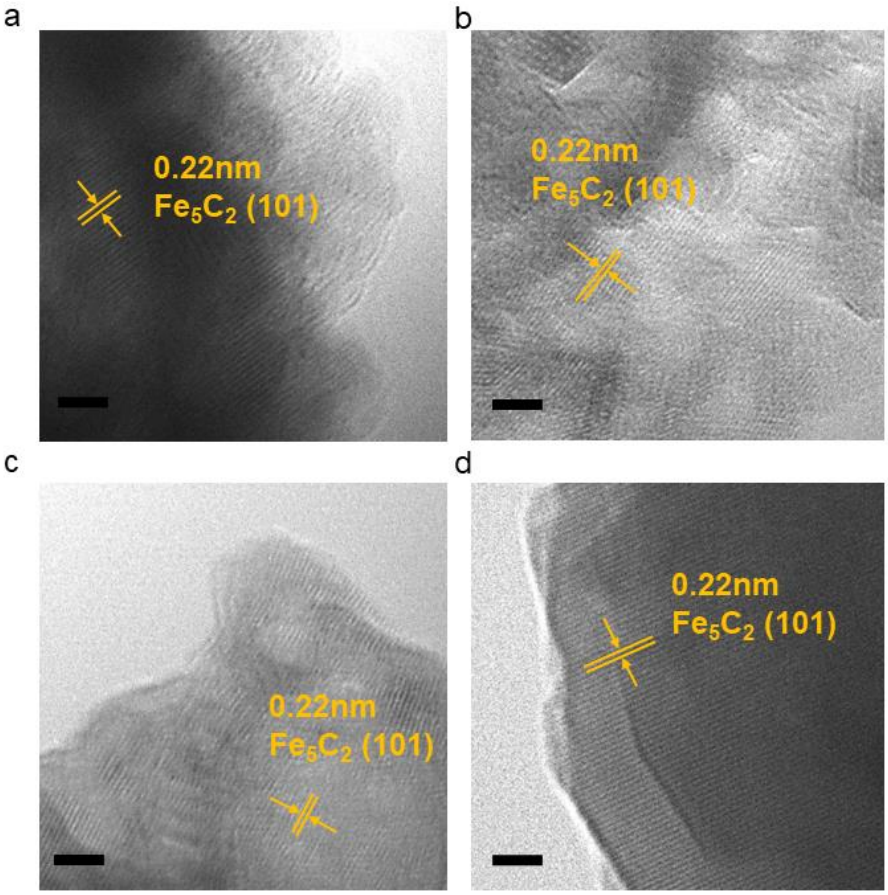

Fig. 1.4 HR-TEM images of spent K-Fe (a), K-6Fe/Zn (b), K-3Fe/Zn (c), K-1Fe/Zn (d); the bars stand for 2 nm.

3.3 Reduction and adsorption behavior of the as-prepared K-nFe/Zn catalysts

H_2-TPR was used to analyze the reduction capacity of the K-nFe/Zn catalysts. Fig. 1.5 compared four H_2-TPR reduction profiles. As seen, two obvious peaks appeared in K-Fe catalyst, which could be ascribed to the reduction processes of Fe_2O_3 to Fe_3O_4 and Fe_3O_4 to metallic Fe. As drawn in Fig. 1.5, a differentiable premature peak (at around 366 °C) appeared compared to K-Fe, which indicated the introduction of Zn promoted the reduction of iron species. Further increasing the ratio of Zn/Fe

could promote the reduction behavior again (K-3Fe/Zn). However, excessive Zn addition caused the reduction peak to shift to a higher temperature, which might be due to the formation of large ZnO clusters and rather stable $ZnFe_2O_4$ species. It could be inferred that the introduction of Zn to iron catalysts played an important role in increasing the iron reducing capability, in which K-3Fe/Zn showed the best reduction ability.

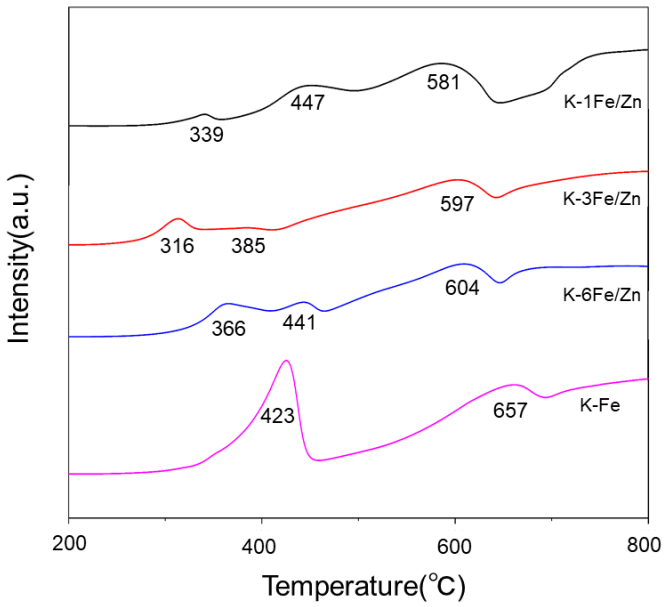

Fig. 1.5 H_2-temperature-programmed reduction (H_2-TPR) profiles of the K-nFe/Zn catalysts.

The adsorption properties of CO_2 molecules over different catalysts were investigated by CO_2-TPD, as depicted in Fig. 1.6. The peak areas could be used to reflect CO_2 adsorption capacities of the catalysts, and the location of the catalyst was used to describe the catalyst's basicity strength, which could affect the RWGS reaction and product distribution. The CO_2 adsorption capability of the K-

nFe/Zn catalysts was summarized in Table 1.4. CO_2 adsorption capacity of the catalyst with the incorporation of Zn was notably higher than that of the K-Fe catalyst without Zn addition, demonstrating that introducing Zn into the catalysts could improve CO_2 adsorption capacity, which would help to boost the CO_2 conversion.

As observed, the desorption peaks of K-6Fe/Zn at 550 °C and 742 °C had a relatively high intensity. However, strong chemisorbed CO_2 molecules (peaks III and IV) over the surface of K-6Fe/Zn could not be able to effectively assist CO_2 hydrogenation and participate RWGS reaction. Previous studies also demonstrated that a desorption peak at a lower temperature (below 450 °C) was favorable to the CO_2 conversion [39]. Among these K-nFe/Zn catalysts, K-3Fe/Zn had the highest content of moderate CO_2 adsorption strength, corresponding to peaks I and II, as listed in Table 1.4. As a result, it is plausible to conclude that K-3Fe/Zn had the greatest potential for promoting CO_2 hydrogenation.

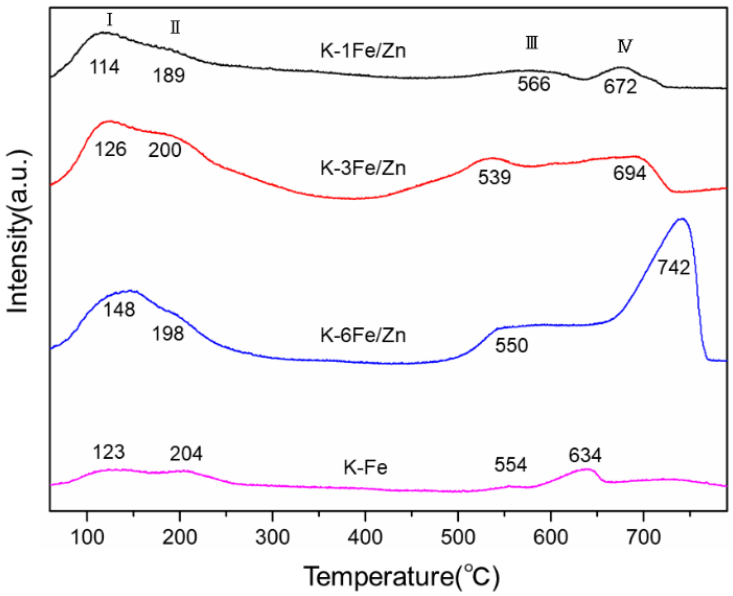

Fig. 1.6 CO_2-temperature-programmed desorption (CO_2-TPD) profiles of K-nFe/Zn catalyst.

Table 1.4 CO_2 uptake amounts of K-nFe/Zn catalyst.

Samples	Total CO_2 uptake amount/mmol/g	CO_2 uptake amount(peak I and II)/mmol/g
K-1Fe/Zn	0.496	0.171
K-3Fe/Zn	0.484	0.192
K-6Fe/Zn	0.649	0.179
K-Fe	0.268	0.082

3.4 Surface phase composition of different K-nFe/Zn catalysts

XPS analysis could be used to determine the composition and content of surface components. Table 1.5 showed the surface element contents calculated from the XPS results. The Fe to Zn molar ratio (4.7) on the catalyst surface was higher than the expected molar ratio in K-3Fe/Zn sample. This was because XPS only identified elements only within 5 nm of the outer surface [40], implying that Zn was largely embedded inside the iron channels and hence difficult to be detected, resulting in a low

Zn surface content. While surface molar ratios of Fe to Zn (5.3 and 0.4) were lower than the intended ratio in the K-6Fe/Zn and K-1Fe/Zn samples, this was attributable to the fact that Zn was concentrated on the catalysts' surfaces, indicating that Zn content influenced the Zn distribution in the K-nFe/Zn catalysts. K/Fe values remained broadly consistent in the 4 catalysts.

Table 1.5 Element content composition obtained from XPS.

Sample	O (at%)	Fe (at%)	Zn (at%)	C (at%)	K (at%)
K-1Fe/Zn	29.58	13.64	36.08	20.07	0.63
K-3Fe/Zn	46.61	20.59	4.35	27.09	0.87
K-6Fe/Zn	49.08	23.50	4.45	21.88	1.09
K-Fe	56.30	27.28	-	15.13	1.29

The phase composition of Fe species in the K-nFe/Zn catalyst was explored using high-resolution XPS. Fig. 1.7 showed the Fe 2p spectra of fresh K-nFe/Zn catalysts. The iron on the surface of the catalysts was composed of Fe^{2+} and Fe^{3+}, as could be seen in XRD in Fig. 1.1. With the addition of Zn, the proportion of Fe^{3+} increased gradually, and the iron species on the K-3Fe/Zn surface mainly consisted of Fe^{3+}. However, further addition of Zn resulted in a reduction in Fe^{3+}. Fig. 1.8 displayed the spent catalysts Fe 2p spectra, and the binding energy peaks at 708.5 eV, 710.2 eV, and 711.3 eV were attributed to Fe-C, Fe^{2+}, and Fe^{3+} species respectively. K-1Fe/Zn and K-3Fe/Zn catalysts had the highest strength of the Fe phase after the reaction, which were consistent with the reaction results in Table 1.7. The binding energy position of Fe-C shifted toward a low binding energy in the four catalysts due to the formation of electron-rich Fe_5C_2 as seen in Fig. 1.1b and Fig. 1.4 [21], which was an active

phase responsible for converting CO_x to hydrocarbons. Meanwhile, Fe-C bond binding energy shifted toward a higher binding energy with the increasing of Zn content, suggesting that the interaction between iron and Zn was enhanced with the increase of Zn, probably because the formation of ZnO changed the iron environment [23].

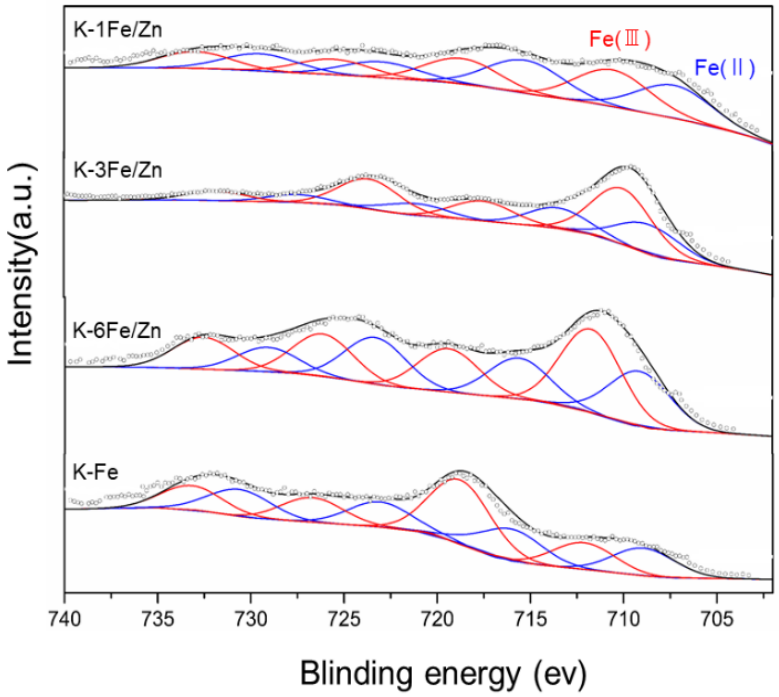

Fig. 1.7 Fe 2p XPS spectra of fresh K-nFe/Zn catalysts.

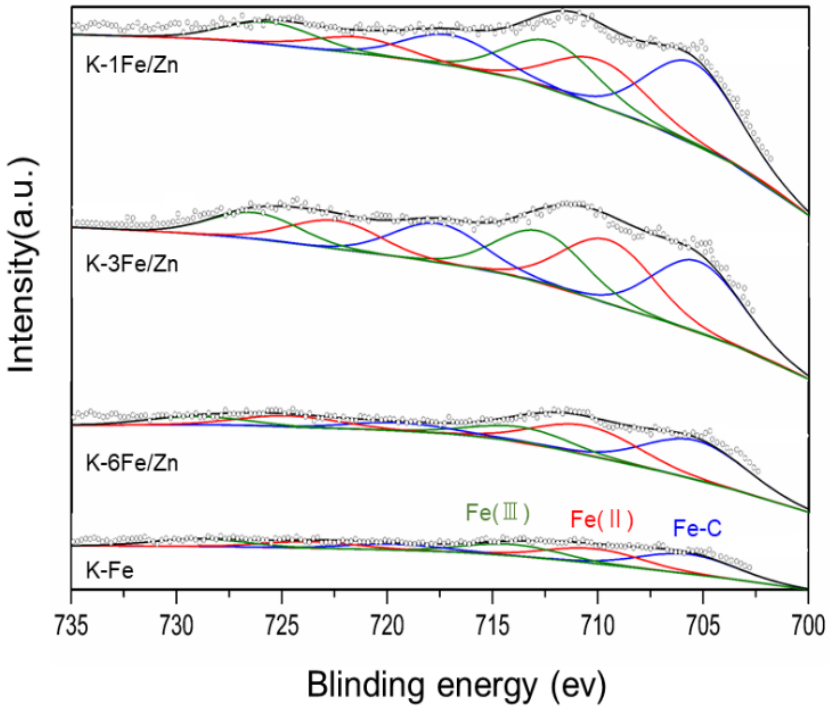

Fig. 1.8 Fe 2p XPS spectra of spent K-nFe/Zn catalysts.

3.5 Characterization of ZSM-5 zeolite catalyst

The XRD patterns of H-ZSM-5 zeolite with different SiO_2/Al_2O_3 ratios were shown in Fig. 1.9. Typical ZSM-5 diffraction peaks were observed in the XRD patterns. Besides, the intensities of the diffraction peaks decreased as the SiO_2/Al_2O_3 ratio decreased.

Fig. 1.10 pictured XRD patterns of H-ZSM-5 (SiO_2/Al_2O_3=21) zeolite treated with NaOH solution of different concentrations. Clearly, the intensities of the XRD diffraction peak decreased with increasing NaOH concentration by destroying partially the original structure of the H-ZSM-5 zeolite. The intensities of the diffraction peaks in the XRD patterns were quite low when the NaOH concentration reached 0.6 M, indicating that the structure of the H-ZSM-5 zeolite was further destroyed.

This result was consistent with the texture properties of parent H-ZSM-5 and NaOH-treated H-ZSM-5, presented in Table 1.6. The specific surface area (m^2/g) was calculated using the Brunauer-Emmett-Teller (BET) method. The average pore size (nm) and pore volume (cm^3/g) were calculated using the Barrett-Joyner-Halenda (BJH) method. As summarized in Table 1.6, zeolites treated with NaOH resulted in the formation of hollow pores. From 0 to 0.2 M, the specific surface area and pore volume of H-ZSM-5 increased. However, as the concentration of NaOH was further increased, the zeolite framework collapsed in a strong alkaline solution, resulting in a reduction in specific surface area.

Table 1.6 Texture properties of H-ZSM-5 (SiO_2/Al_2O_3=21) treated by various concentrations of NaOH.

Catalyst	$S_{BET}(m^2/g)$	Pore diameter (nm)	Pore volume(cm^3/g)
H-ZSM-5-0M	300.21	13.96	0.17
H-ZSM-5-0.1M	306.38	14.62	0.16
H-ZSM-5-0.2M	355.37	16.88	0.19
H-ZSM-5-0.4M	410.50	19.58	0.21
H-ZSM-5-0.6M	369.90	25.63	0.47

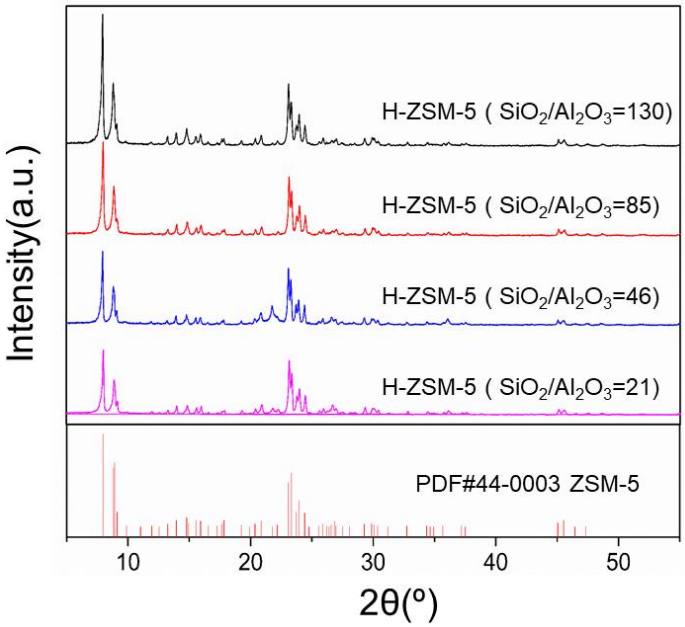

Fig. 1.9 XRD patterns and PDF cards of H-ZSM-5 zeolite with different SiO_2/Al_2O_3 ratios.

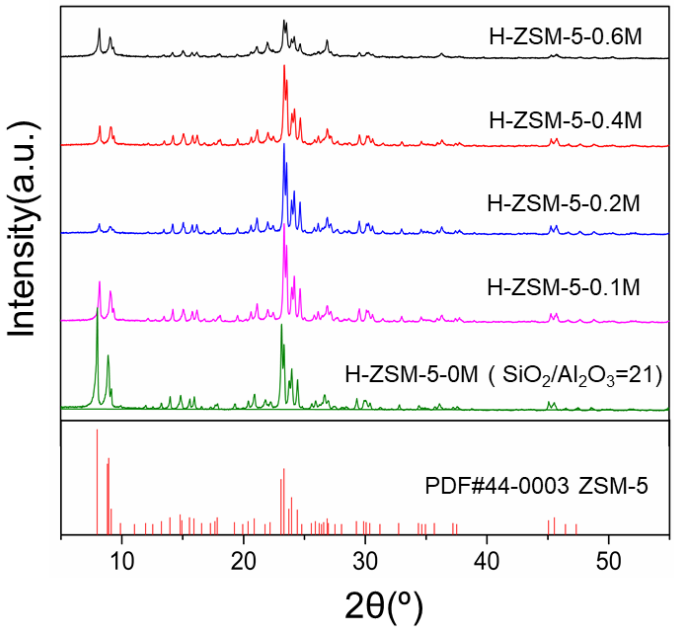

Fig. 1.10 XRD patterns and PDF cards of H-ZSM-5 (SiO_2/Al_2O_3=21) zeolite treated with different concentrations of NaOH solution.

Fig. 1.11 depicted the NH_3-TPD profiles of different zeolites, which were used to investigate the difference in acidic properties of NaOH treated H-ZSM-5. With increasing NaOH content, typical NH_3 desorption peaks shifted toward higher temperatures, indicating an increase in acid strengths and densities after alkali solution treatment.

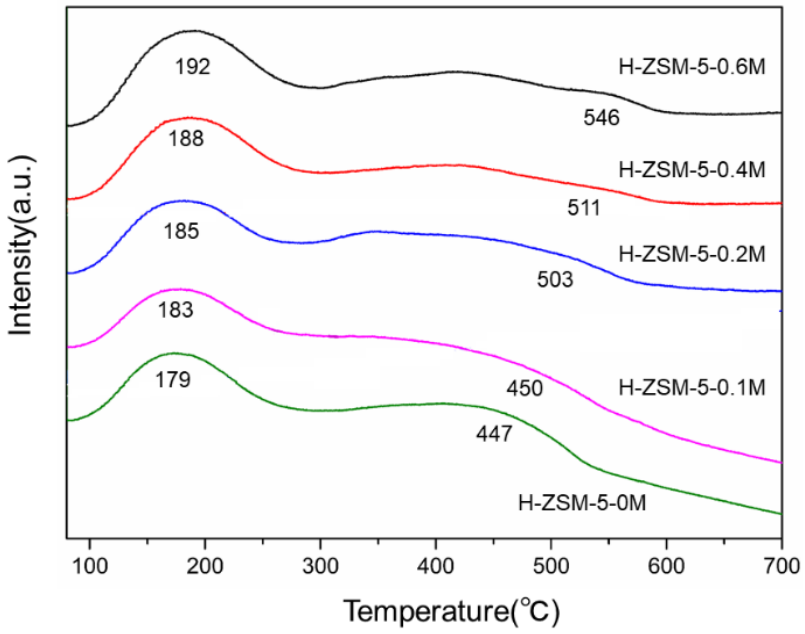

Fig. 1.11 NH_3-TPD profiles of H-ZSM-5-X.

SEM images of parent H-ZSM-5 and H-ZSM-5 following NaOH treatment are shown in Fig. 1.12. H-ZSM-5 progressively bonded together and lost its zeolite morphology as the NaOH solution concentration increased, as seen by the decreasing strength of the XRD diffraction peak (Fig. 1.10).

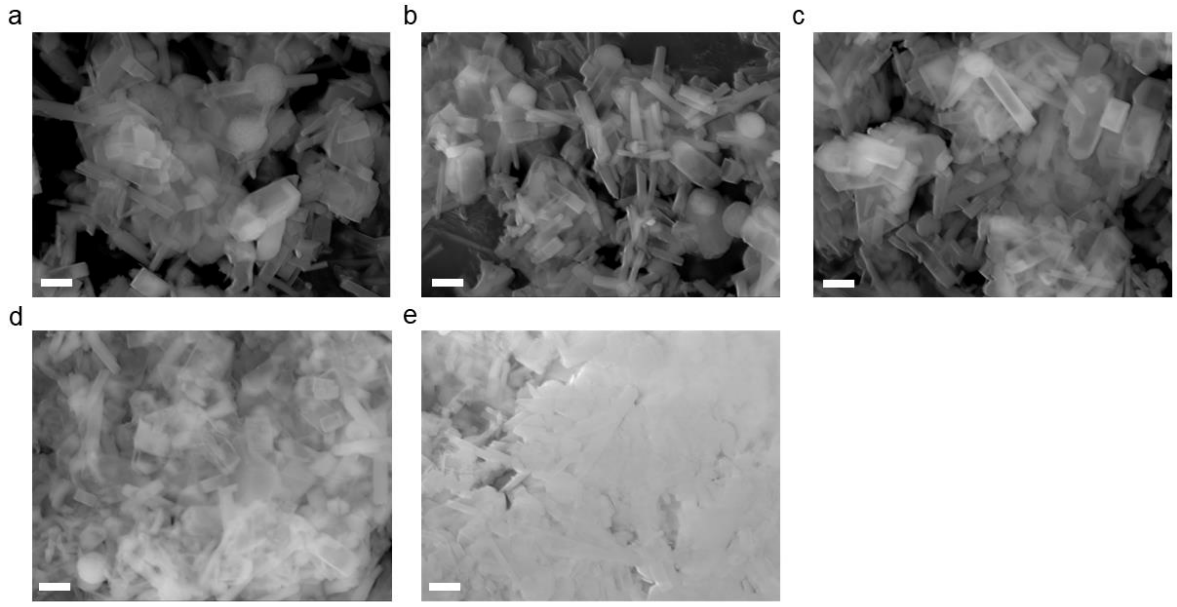

Fig. 1.12 SEM images of parent H-ZSM-5 (SiO_2/Al_2O_3=21) (a), H-ZSM-5-0.1M (b), H-ZSM-5-0.2M (c), H-ZSM-5-0.4M (d), H-ZSM-5-0.6M (e); the bars stand for 1 μm.

3.6 Catalytic performances of the K-nFe/Zn and composite catalysts

CO_2 hydrogenation performances over different catalysts were conducted and the results were summarized in Table 1.7. Compared to the K-Fe sample without Zn promotion, the catalytic activity increased slightly over the K-6Fe/Zn catalyst which maintained a low CH_4 selectivity. With the further increase of Zn content, the catalytic activity presented a volcanic increase and reached the maximum over K-3Fe/Zn catalyst. By contrary, undesired CO and CH_4 selectivities reached minimum value (Table 1.7). Different groups reported that the incorporation of Zn aided the production of light hydrocarbons, and the formation of ZnO promoted the RWGS reaction, which increased the CO_2 conversion [23]. However, excessive addition of Zn resulted in a decrease in catalytic activity and an

increase in undesired CH_4 selectivity. This could be explained by the extreme production of unreducible ZnO in the iron species precursors, as observed in the XRD results (Fig. 1a), which prevented the catalysts from activation, resulting in a decrease in activity during CO_2 hydrogenation. Catalytic stability of K-3Fe/Zn was tested for 80 h and the result was shown in Fig. 1.13, the activity of K-3Fe/Zn remained basically stable in 80 hours, indicating that K-3Fe/Zn had a good stability.

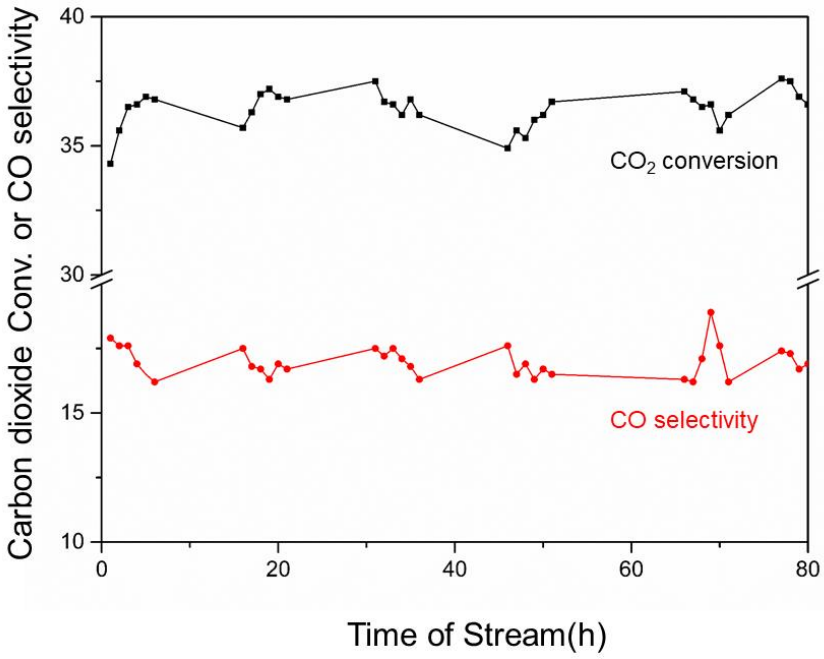

Fig. 1.13 Catalytic stability of K-3Fe/Zn catalyst. Reaction conditions: 320 ℃, 3.0 MPa, $H_2/CO_2/Ar$=68.0%: 27.0%: 5.%, TOS＝8 hours, W/F= 3 $g \cdot h \cdot mol^{-1}$.

Table 1.7 Catalytic performances of K-nFe/Zn catalysts for CO_2 hydrogenation.[a]

Catalysts	CO_2 Conv. (%)	CO Sel. (%)	Selectivity (%)					
			CH_4	C_2-C_4^{p} [b]	C_2-$C_4^{=}$ [b]	C_4^{iso} [b]	C_5^{+} [c]	aromatics
K-1Fe/Zn	33.2	17.6	24.6	4.6	29.0	0.5	40.2	1.1
K-3Fe/Zn	36.6	16.7	16.3	3.7	27.6	0.7	50.4	1.3
K-6Fe/Zn	31.3	20.3	18.6	6.2	23.9	0.8	49.8	0.7
K-Fe	28.2	24.4	26.6	6.0	22.9	0.7	43.3	0.5

a Reaction conditions: 320 ℃, 3.0 MPa, $H_2/CO_2/Ar$=68.0%: 27.0%: 5.0%, TOS＝8 hours, W/F= 3 $g \cdot h \cdot mol^{-1}$.

b C_2–C_4^{p} means C_2–C_4 paraffin

C_2–$C_4^{=}$ means C_2–C_4 olefin

C_4^{iso} means C_4 isoparaffin.

c C_5^{+} hydrocarbons without aromatics.

The original H-ZSM-5 zeolites with various SiO_2/Al_2O_3 ratios of 130, 85, 46 and 21 were also combined with K-3Fe/Zn to obtain hybrid catalysts for CO_2 hydrogenation. As presented in Table 1.8, the composite catalysts could convert CO_2 molecules into aromatics. With a decrease in the SiO_2/Al_2O_3 ratio from 130 to 21, the aromatic selectivity increased from 10.5% to 25.4% and the light olefins selectivity decreased from 21.1 to 12.9%, indicating that when the SiO_2/Al_2O_3 ratio was 21, more light olefins were converted to aromatics. This finding supported the theory that the Brönsted acidity of the H-ZSM-5 zeolite was a critical component in the aromatization process [17]. In addition, CO_2 conversion and CO selectivity improved when the SiO_2/Al_2O_3 ratio decreased from 130 to 21. In conclusion, the SiO_2/Al_2O_3 ratio of 21 not only corresponded to the best aromatic selectivity but also resulted in the highest CO_2 conversion and the lowest CO selectivity. It also had been reported that treating zeolite with NaOH solution could form a hollow structure in the zeolite channel, greatly

reducing the residual time of aromatic intermediates in the channel, which not only improved the synthesis efficiency of aromatic hydrocarbons but also prevented overhydrogenation of hydrocarbons in the channel. Thus, a zeolite with a SiO_2/Al_2O_3 ratio of 21 was modified with NaOH to further improve aromatic selectivity.

Table 1.8 Catalytic performances of hybrid catalysts prepared by combining K-3Fe/Zn with varied H-ZSM-5.[a]

H-ZSM-5 with varied SiO_2/Al_2O_3	CO_2 Conv. (%)	CO Sel. (%)	Selectivity (%)					
			CH_4	C_2-C_4^p	C_2-$C_4^=$	C_4^{iso}	C_5^{+} [b]	aromatics
130	31.2	16.0	15.7	5.2	21.1	2.2	45.3	10.5
85	39.3	14.1	15.5	5.8	19.3	3.5	42.2	13.7
46	35.3	12.8	14.2	6.5	15.8	2.9	38.8	21.8
21	43.6	11.5	13.6	7.2	12.9	3.2	37.7	25.4

a Reaction conditions: 320 ℃, 3.0 MPa, $H_2/CO_2/Ar$=68.0 : 27.0 : 5.0, TOS＝8 hours, W/F= 6 $g \cdot h \cdot mol^{-1}$, weight ratio of K-3Fe/Zn to H-ZSM-5 is 1:1.
b C_5^+ hydrocarbons without aromatics.

As shown in Table 1.9, catalytic performances were also conducted over a tailor-made zeolite (SiO_2/Al_2O_3=21) which treated by various NaOH solution concentration (0.1 M, 0.2 M, 0.4 M, or 0.6 M). Clearly, by increasing the NaOH concentration from 0 to 0.1 M to 0.2 M, the selectivity of the aromatics increased gradually from 25.4% to 27.9% and then to 35.1%. This phenomenon could be ascribed to that H-ZSM-5 treated with 0.1 M and 0.2 M NaOH exhibited improved mass-transfer efficiency of the intermediates during the catalysis process. Furthermore, 0.1 and 0.2 M NaOH could regulate H-ZSM-5's acidic property by dispersing Al species within the zeolite skeleton (Fig. 1.11). As

a result, more light olefins were converted into aromatics inside H-ZSM-5-0.1M and H-ZSM-5-0.2M. However, further increasing the NaOH concentration to 0.4 M and 0.6 M resulted in a decrease in the aromatic selectivity to 20.1% and 15.3%, respectively. This could be explained that zeolite structural degradation was induced by high NaOH concentrations, which was demonstrated in Fig 1.10–12. Besides, the selectivity of PX, as an important chemical product, reached as high as 8.2% in all aromatics in K-3Fe/Zn/H-ZSM-5-0.2M catalyst (Table 1.10). Consequently, it could be concluded that the best catalyst for effective CO_2 conversion to aromatics here was K-3Fe/Zn + H-ZSM-5-0.2M (SiO_2/Al_2O_3=21). Detailed hydrocarbon distribution over K-3Fe/Zn and K-3Fe/Zn and H-ZSM-5-0.2 M bifunctional catalysts has been added as Fig. 1.14. The results indicated that olefins were converted into aromatics especially lower carbon olefins.

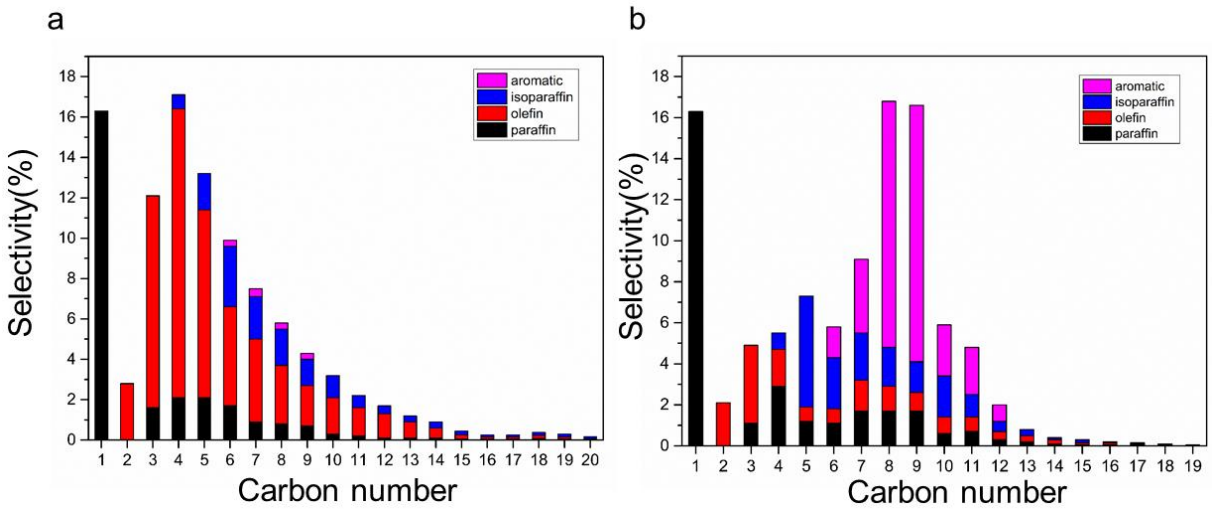

Fig. 1.14 Detailed hydrocarbon distribution over K-3Fe/Zn (a) and K-3Fe/Zn and H-ZSM-5-0.2M bifunctional catalysts (b). Reaction conditions: 320 ℃, 3.0 MPa, $H_2/CO_2/Ar$=68.0%: 27.0%: 5.0%,

TOS＝8 hours, W/F= 3 g·h·mol^{-1} and 6 g·h·mol^{-1}.

Table 1.9 Catalytic performances of hybrid catalysts prepared by combining K-3Fe/Zn with NaOH treated H-ZSM-5.[a]

Varied NaOH solution concentration(mol/L)	CO_2 Conv. (%)	CO Sel. (%)	Selectivity (%)					
			CH_4	C_2-C_4^p	C_2-$C_4^=$	C_4^{iso}	C_5^{+} [b]	aromatics
0.1	43.6	8.2	17.7	2.4	14.3	0.6	37.1	27.9
0.2	44.2	10.1	16.3	2.0	9.7	0.8	36.1	35.1
0.4	40.6	14.2	19.6	4.6	15.2	1.0	39.5	20.1
0.6	42.4	16.0	20.9	5.3	17.7	0.5	40.3	15.3

a Reaction conditions: 320 ℃, 3.0 MPa, $H_2/CO_2/Ar$=68.0%: 27.0%: 5.0%, TOS＝8 hours, W/F= 6 g·h·mol^{-1}, weight ratio of K-3Fe/Zn to H-ZSM-5 is 1:1, original SiO_2/Al_2O_3 is 21.
b C_5^+ hydrocarbons without aromatics.

Table 1.10 Distribution of aromatics hydrocarbons in K-3Fe/Zn & H-ZSM-5-0.2M catalytic performance.[a]

B^b (%)	T^b (%)	E^b (%)	OX^b (%)	MX^b (%)	PX^b (%)	A^b (C_9) (%)	A^b (C_{10}^+) (%)
4.2	10.2	5.9	7.5	12.5	8.2	35.5	16.0

a Reaction conditions: 320 ℃, 3.0 MPa, $H_2/CO_2/Ar$=68.0: 27.0: 5.0, 0.25g K-Fe/Zn (20–40 meshes) + 0.25g H-ZSM-5 (20–40 meshes), TOS＝8 hous, F=30 mL/min
b B means benzene.
T means Toluene.
E means Ethylbenzene.
OX means O-xylene.
MX means M-xylene.
PX means P-xylene.

In order to further study the selectivity relationship between the employed amount of zeolites and aromatics selectivity, the activities of composite catalysts containing different proportions of K-3Fe/Zn and H-ZSM-5 were evaluated. The catalytic performance was presented in Table 1.11. When the

weight of H-ZSM-5 increased from 0.25 g to 0.75 g, the selectivity of the aromatics increased from 35.1% to 45.2%. This was due to the utilization of additional Brönsted acid sites in the conversion of light olefins to aromatics. However, further increasing the H-ZSM-5 weight to 1.0 g resulted in a decrease in the aromatic selectivity because the overhydrocracking reaction on the increased Brönsted acid sites produced more CH_4 and isoparaffins. In addition, the extra acid sites might surround the Fe particles which would inhibit the carburization of the Fe species [26], as a result there was a decrease in CO_2 conversion with the ratio of K-3Fe/Zn to H-ZSM-5-0.2M decreased.

Table 1.11 Catalytic performance of hybrid catalysts prepared by different weight ratio of K-3Fe/Zn to NaOH treated H-ZSM-5.[a]

Varied ratio (K-3Fe/Zn to H-ZSM-5-0.2M)	CO_2 Conv. (%)	CO Sel. (%)	Selectivity (%)					
			CH_4	C_2-C_4^p	C_2-$C_4^=$	C_4^{iso}	C_5^{+} [b]	aromatics
1:1	46.0	8.3	16.3	2.0	9.7	0.8	36.1	35.1
1:2	43.0	10.2	12.1	3.1	7.2	1.0	35.2	41.4
1:3	42.6	10.1	12.5	3.2	6.9	1.1	31.1	45.2
1:4	40.1	10.6	20.7	6.7	12.8	3.1	24.8	31.9

a Reaction conditions: 320 ℃, 3.0 MPa, $H_2/CO_2/Ar$=68.0: 27.0: 5.0, TOS＝8 hours, W/F= 6 g·h·mol^{-1}.

b C_5^+ hydrocarbons without aromatics.

4. Conclusion

K-nFe/Zn catalysts were successfully developed to convert CO_2 into light alkenes. Thereinto, with the addition of Zn, the catalyst's reduction and CO_2 adsorption capacity were improved. When

the Fe/Zn ratio was 3, the catalyst exhibited the best overall ability. K-3Fe/Zn was then combined with H-ZSM-5 with various SiO_2/Al_2O_3 ratios for CO_2 to aromatics. When the SiO_2/Al_2O_3 was 21, the composite catalyst presented the highest aromatics selectivity (25.4%). To increase the transport efficiency of the aromatic precursors in the brizeolite channel, H-ZSM-5 was further treated with NaOH solution to improve target aromatics selectivity. When the concentration of NaOH solution was 0.2 M, the aromatic selectivity reached a maximum (35.1%). However, further increasing the concentration of NaOH could collapse the zeolite structure, thus decreasing aromatic selectivity. Furthermore, the relationship between zeolite weight and aromatic selectivity was investigated, discovering that when the weight ratio of the zeolite to K-3Fe/Zn increased from 1:1 to 3:1, the aromatic selectivity reached its maximum (45.2%). However, excessive unitization of zeolite resulted in an overhydrocracking reaction owing to the increased Brönsted acid sites, thus decreasing the aromatic selectivity. In summary, an efficient composite catalyst could be rationally constructed by regulating component composition and the microenvironment of zeolite for directly converting CO_2 into aromatics.

References

(1) R, Ye. et al. CO_2 hydrogenation to high-value products via heterogeneous catalysis. *Nature Commun.* **10**, 5698 (2019).

(2) C, Hepburn. et al. The technological and economic prospects for CO_2 utilization and removal. *Nature.* **575**, 87–97 (2019).

(3) G.A, Olah. et al. Anthropogenic chemical carbon cycle for a sustainable future. *J. Am. Chem. Soc.* **133**, 12881–12898 (2011).

(4) Zhou, W. et al. New horizon in C_1 chemistry: breaking the selectivity limitation in transformation of syngas and hydrogenation of CO_2 into hydrocarbon chemicals and fuels. *Chem. Soc. Rev.* **48**, 3193–3228 (2019).

(5) Zhu, P. et al. Tandem catalytic synthesis of benzene from CO_2 and H_2. *Catal. Sci. Technol.* **7**, 2695–2699 (2017).

(6) Dong, X. et al. CO_2 hydrogenation to methanol over Cu/ZnO/ZrO_2 catalysts prepared by precipitation-reduction method. *Appl. Catal. B-Environ.* **191**, 8–17 (2016).

(7) Frusteri, F. et al. Stepwise tuning of metal-oxide and acid sites of CuZnZr-MFI hybrid catalysts for the direct DME synthesis by CO_2 hydrogenation. *Appl. Catal. B-Environ.* **176–177**, 522–531 (2015).

(8) Álvarez, A. et al. Challenges in the Greener Production of Formates/Formic Acid, Methanol, and DME by Heterogeneously Catalyzed CO_2 Hydrogenation Processes. *Chem. Rev.* **117**, 9804–9838 (2017).

(9) Federsel, C. et al. State-of-the-Art Catalysts for Hydrogenation of Carbon Dioxide. *Angew. Chem. Int. Ed.* **49**, 6254–6257 (2010).

(10) Wang, X. et al. Synthesis of Isoalkanes over a Core (Fe−Zn−Zr) −shell (Zeolite) Catalyst by CO_2 Hydrogenation. *Chem. Commun.* **52**, 7352–7355 (2016).

(11) Zhou, C et al. Highly Active ZnO-ZrO_2 Aerogels Integrated with H-ZSM-5 for Aromatics Synthesis from Carbon Dioxide. *ACS Catal.* **10**, 302–310 (2020).

(12) Gao, W. et al. Capsule-like zeolite catalyst fabricated by solvent-free strategy for para-Xylene formation from CO_2 hydrogenation. *Appl. Catal. B-Environ.* **303**, 120906 (2022).

(13) Zhang, P. et al. One-pass selective conversion of syngas to para-xylene. *Chem. Sci.* **8**, 7941–7946 (2017).

(14) Niziolek, A.M. et al. Biomass-based production of benzene, toluene, and xylenes via methanol: process synthesis and deterministic global optimization. *Energy Fuels.* **30**, 4970–4998 (2016).

(15) Ni, Y. et al. Selective conversion of CO_2 and H_2 into aromatics. *Nature Commun.* **9**, 3457 (2018).

(16) Wang, Y. et al. Direct and oriented conversion of CO_2 into value-added aromatics. *Chem. Eur. J.* **25**, 5149–5153 (2019).

(17) Wang, Y. et al. Direct conversion of CO_2 to aromatics with high yield via a modified Fischer-Tropsch synthesis pathway. *Appl. Catal. B-Environ.* **269**, 118792 (2020).

(18) Wang, Y. et al. Rationally designing bifunctional catalysts as an efficient strategy to boost CO_2 hydrogenation producing value-added aromatics. *ACS Catal.* **9**, 895–901 (2019).

(19) Gnanamani, M.K. et al. Hydrogenation of carbon dioxide over Co-Fe bimetallic catalysts. *ACS Catal.* **6**, 913–927 (2016).

(20) Cheng, K et al. Direct and highly selective Conversion of Synthesis Gas into Lower Olefins: Design of a Bifunctional Catalyst Combining Methanol Synthesis and Carbon-Carbon Coupling. *Angew, Chem.* **128**, 4803–4806 (2016).

(21) Guo, L. et al. Spinel-structure catalyst catalyzing CO_2 hydrogenation to full spectrum alkenes with an ultra-high yield. *Chem. Commun.* **56**, 9372–9375 (2020).

(22) Kasol, R. et al. Iron catalysts supported on nitrogen functionalized carbon for improved CO_2 hydrogenation performance. *Catal. Commun.* **149**, 106216 (2021).

(23) Zhang, J. et al. Selective formation of light olefins from CO_2 hydrogenation over Fe–Zn–K catalysts. *J. CO_2. Util.* **12**, 95–100 (2015).

(24) Wang, Y et al. Visualizing Element Migration over Bifunctional Metal-Zeolite Catalysts and its Impact on Catalysis. *Angew. Chem. Int. Ed.* **60**, 17735–17743 (2021).

(25) Wang, N. et al. Modulation of b-axis thickness within MFI zeolite: correlation with variation of product diffusion and coke distribution in the methanol-to-hydrocarbons conversion. *Appl. Catal. B-Environ.* **243**, 721–733 (2019).

(26) Xu, Y. et al. Conversion of syngas toward aromatics over hybrid Fe-based Fischer-Tropsch catalysts and HZSM-5 zeolites. *Appl. Catal. A: Gen.* **552**,168–183 (2018).

(27) He, J. et al. Controlled fabrication of mesoporous ZSM-5 zeolite-supported PdCu alloy

nanoparticles for complete oxidation of toluene. *Appl. Catal. B-Environ.* **265**, 118560 (2020).

(28) Donk, S. V. et al. Generation, Characterization, and Impact of Mesopores in Zeolite Catalysts. *Catal. Rev.* **45**, 297–319 (2003).

(29) Kustova, M. Y. et al. Direct NO decomposition over conventional and mesoporousCu-ZSM-5 and Cu-ZSM-11 catalysts: Improved performance with hierarchical zeolites. *Appl. Catal. B-Environ.* **67**, 60–67 (2006).

(30) Groen, J. C. et al. Mesoporosity development in ZSM-5 zeolite upon optimized desilication conditions in alkaline medium. *Colloid. Surface. A.* **241**, 53–58 (2004).

(31) Groen, J. C. et al. Optimal aluminum-assisted Mesoporosity development in MFI zeolites by Desilication. *J. Phys. Chem. B.* **108**, 13062–13065 (2004).

(32) Groen, J. C. et al. Creation of hollow zeolite architectures by controlled desilication of Al-Zoned ZSM-5 crystals. *J. Am. Chem. Soc.* **127**, 10792–10793 (2005).

(33) Bjørgen, M. et al. Methanol to gasoline over zeolite H-ZSM-5: Improved catalyst performance bytreatment with NaOH. *Appl. Catal. A-Gen.* **345**, 43–50 (2008).

(34) Fathi, S. et al. Improvement of HZSM-5 performance by alkaline treatments: Comparative catalytic study in the MTG reactions. *Fuel.* **116**, 529–537 (2014).

(35) Guo, L. et al. One-Pot Hydrothermal Synthesis of Nitrogen Functionalized Carbonaceous Material Catalysts with Embedded Iron Nanoparticles for CO_2 Hydrogenation. *ACS. Sustain. Chem. Eng.* **7**, 8331–8339 (2019).

(36**)** Li, S. et al. Effects of Zn, Cu, and K Promoters on the Structure and on the Reduction, Carburization, and Catalytic Behavior of Iron-Based Fischer–Tropsch Synthesis Catalysts. *Catal. Lett.* **77**, 197–205 (2001).

(37**)** Wang, H. et al. Study of bimetallic interactions and promoter effects of FeZn, FeMn and FeCr Fischer–Tropsch synthesis catalysts. *J. Mol. Catal. A-Chem.* **326**, 29–40 (2010).

(38) Lyu, S. et al. Stabilization of ε-iron carbide as high-temperature catalyst under realistic Fischer–Tropsch synthesis conditions. *Nature Commun.* **11**, 6219 (2020).

(39) Wang, J. et al. Synthesis of lower olefins by hydrogenation of carbon dioxide over supported iron catalysts. *Catal. Today.* **215**, 186–193 (2013).

(40) Liu, G. et al. Nitrogen-rich mesoporous carbon supported iron catalyst with superior activity for Fischer-Tropsch synthesis. *Carbon.* **130**, 304–314 (2018).

Chapter 2

In Situ Quick Microwave Assembling Nitrogen-Regulated Graphene Supported Iron Nanoparticles for Fischer-Tropsch Synthesis

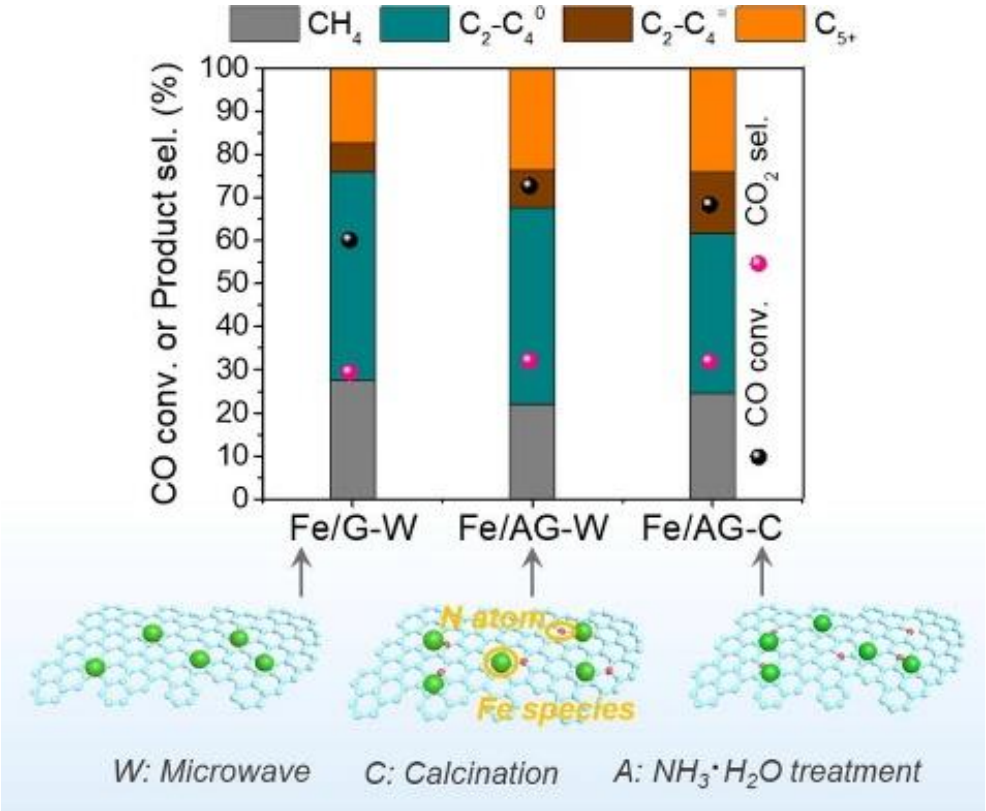

Abstract

Facile preparation of highly efficient iron-based catalyst is vital to improve the performance of Fischer-Tropsch synthesis, a sustainable process for converting non-petroleum carbon resources to valuable hydrocarbons. Herein, we report a convenient method for the preparation of nitrogen-regulated graphene supported iron nanoparticles through the help of microwave treatment, in which the nitrogen-containing groups in support were introduced by $NH_3 \cdot H_2O$ treatment. The introduction of a small number of nitrogen-containing groups could effectively anchor iron species, increase the surface alkalinity of the catalyst, and thus promote the formation of small iron species under heating conditions, which has an important effect on the improvement of catalytic activity. Meanwhile, the supported iron sizes of the catalysts from 120 nm to 10 nm could be well regulated via tuning the microwave heating time. The existences of small-size iron species were conducive to CO conversion (96.2%). In addition, the duration length of $NH_3 \cdot H_2O$ treatment time could not only increase the content of nitrogen-containing groups, but also regulate the configuration of N species in the support materials, thus affecting the catalytic performance. As a result of the superior preparation and catalytic performance, the catalyst could be one of ideal candidates for iron-based FTS catalysts in the future.

Keywords: Fischer-Tropsch synthesis; Iron catalysts; Graphene; Nitrogen modification; Microwave treatment

1. Introduction

With the increasing depletion of fossil sources and the emphasis on sustainable development, tremendous attention has been paid to the alternative feed stocks. Thereinto, Fischer-Tropsch synthesis (FTS) is regarded as a promising strategy through utilizing various feedstocks such as natural gas, coal, and biomass, to substitute the petroleum-based chemicals or fuels. Although the FTS process has been studied nearly 100 years, the catalysts used in this process have been optimized by academia and industry and have attracted considerable worldwide attention [1–3]. To be specific, FTS can be performed on an iron(Fe)-based, cobalt(Co)-based, or ruthenium(Ru)-based catalyst, with the supported Fe-based catalysts being preferred owing to the wide utilization range of H_2/CO ratio (such as biomass-derived syngas), wide operation temperature, and low cost in comparison with the Co-based or Ru-based catalysts [4, 5]. As a consequence, rational design or/and facile synthesis of an efficient Fe-based catalyst has been a central issue to achieve an excellent FTS performance.

Support materials can promote the dispersion of active phase, which can make the catalyst present a benign catalytic performance. Common support materials include Al_2O_3, SiO_2, zeolite, and other inorganic materials [5]. The utilization of these inorganic materials easily lead to the formation of a hardly reducible iron species (for example, iron silicates), which is not conducive to the generation of active sites. Different from these support materials above, carbon-based support materials especially graphene have been widely studied and used in heterogeneous catalysis field in recent years [6–9]. Particularly, promising carbon materials usually exhibit weak metal-support interaction which favors

metal reduction and enhances catalytic activity. Sun et al. synthesized an efficient Fe_2O_3 nanoparticles with graphene as support through one-pot hydrothermal hydrolysis-reduction strategy, and the catalysts showed a favorable stability and liquid hydrocarbon selectivity [6]. Similarly, Wei et al. fabricated a hierarchically mesoporous iron oxide/graphene catalyst, displaying remarkably high FTS performance [10]. Moussa et al. found that Fe nanoparticles supported on graphene support also showed good catalytic performance, in which the benign performance was correlated with graphene lattices acting as favorable sites to anchor the Fe nanoparticles (NPs) [11]. Moreover, the catalytic activity of FTS process over a graphene-encapsulated Fe NPs was more than three times that of bare Fe NPs [12]. Besides, it was reported that the interaction between Fe and graphene oxide support can be controlled by adjusting the pretreatment calcination operation, thus achieving high FTS activity and C_{5+} selectivity [13]. It could be expected that graphene, as a promising alternative support, has nice research and application prospects.

Generally, bare Fe catalysts without any modification present an inferior catalytic activity as well as target products selectivity. To further boost the catalytic performance of FTS, various treatments were adopted such as electron promoters (K, Mg, Mn, Na, Cu, etc.) doping into the Fe-based catalysts [14–18]. Recently, the emerging tactics of nitrogen (N) doping for carbon materials provided a promising strategy for improving catalytic performance, as with metal promoter modification. The incorporation of N atom into carbon support materials regulated surface basicity and chemical properties of catalysts, being dedicated to enhance catalytic performance of FTS [19–21]. Lee et al.

prepared a carbon encapsulated iron-carbides supported on N-doped porous carbon (Fe_5C_2@C/NPC) catalyst, showing high hydrocarbon productivity and up to 96% CO conversion [22]. Schulte et al. reported that iron nanoparticles supported on nitrogen-functionalized carbon nanotubes resulted in a higher intrinsic activity as well as stability [23]. Lu et al. demonstrated that superior FTS performance determined by dissociative CO adsorption and active iron carbides formation could be achieved by means of anchoring effect and the intrinsic basicity of N participation [24]. Similarly, it was reported that N atoms acting as electron donors promoted the dissociation of CO and expedited the formation of carbides, thus achieving high FTS activity [21, 25]. N atoms in graphene support could offer the electron and keep the iron particles at a low valence state in a manner similar to the promotional effect of alkali metal promoters utilization [26]. In addition to the electronic effect of N atoms, the strong surface basicity resulted from N doping was another crucial factor for improving FTS performance [20]. It is obvious that N atoms doping modification in carbon support is helpful for the preparation of an efficient iron based catalyst.

Herein, we reported a facile *in situ* engineering method for making N-doped graphene supported iron NPs. This was accomplished using a microwave treatment with a solid precursor under the protection of nitrogen atmosphere (Scheme 2.1). It was worth noting that the catalyst was not processed by traditional heating equipment (for example, calcination) during the preparation process and the preparation cycle was rather shorter than conventional processes. With the incorporation of N atoms, catalytic activity was obviously enhanced and the conversion was as high as 97%, which was higher

than conventional catalyst systems. N-doped graphene supported iron NPs assisted by microwave treatment open a promising route for the development of advanced FTS catalysts.

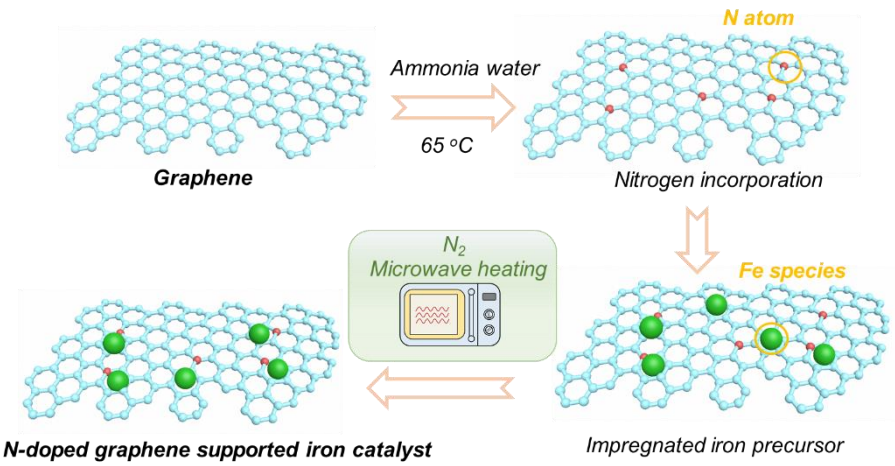

Scheme 2.1 Synthesis route of nitrogen-regulated graphene supported iron nanoparticles via a facile microwave heating method.

2. Experimental section

2.1 Catalyst preparation

Graphene nanoplatelets aggregates (sub-micron particles, surface area 300 m^2/g) were purchased from FUJIFILM Wako Pure Chemical Corporation, marked as G. The G was then modified with N atoms. Specifically, $NH_3 \cdot H_2O$ of 10 g was added to suspension of 50 mL (10 g GO /L^{-1}), heating at 65 °C for X hours, and then filtered and washed to get a graphene support containing-nitrogen groups, labelled as AG (Xh). Y wt% loading of iron was introduced into support via an impregnation method. It was then vacuum dried at 80 °C for 10 hours. The obtained catalyst was treated with microwave for

Z seconds under the protection of N_2 atmosphere (using 700W microwave oven). In terms of Y wt%Fe/AG(Xh) and Y wt%Fe/AG-W(Z), X denotes $NH_3 \cdot H_2O$ treatment time, Y denotes the loading of iron, and Z denotes microwave treatment time. In addition, the symbol of W stands for microwave treatment. In order to elevate the advantage of microwave treatment, a reference catalyst calcinated by muffle furnace was fabricated. And when W was replaced by C, it means calcination treatment, such as Fe/AG-C. To be specific, 5 wt% loading of iron was first introduced into support through impregnation method, and then vacuum dried at 80 °C for 10 hours. Thereinto, the support was treated by $NH_3 \cdot H_2O$ at 65 ºC for 6 hours. The obtained catalyst was treated with muffle furnace (550 ºC, 3 hours) with the protection of N_2 atmosphere. In terms of Fe/AG-W, iron loading was 5wt%, and it was treated with microwave heating for 6 seconds under 700-W condition. In particular, if there was no number in the parentheses after the W, the default value for microwave treatment was 6 seconds.

2.2 Catalyst characterization

X-ray diffraction (XRD) spectra of the powder catalysts were collected using a Rigaku RINT 2400 X-ray Diffractometer (Cu-Ka, 40 kV, 40 mA). Scans were recorded in the 2θ range of 5˚–90˚ with a step size of 0.02˚/s. N_2 physisorption isotherms were measured at -196 ºC by using a NOVA 2200e apparatus. Before the N_2 adsorption, the catalysts were degassed under vacuum at 200 ºC for 6 hours. H_2 temperature programmed reduction (H_2-TPR) and CO_2 temperature programmed desoption (CO_2-TPD) were studied using a BELCAT-II-T-SP analyser. X-ray photoelectron spectroscopy (XPS)

analysis was conducted using a Thermo Fisher Scientific ESCALAB 250Xi multifunctional X-ray photoelectron instrument. The transmission electron microscope (TEM, JEOL JEM-3200Fs) was employed to observe the particle size and distribution at an acceleration voltage of 100 kV. The ^{57}Fe Mössbauer spectra of the spent catalysts were recorded at room temperature over a Topologic 500A spectrometer and a proportional counter. Magnetic hyperfine field was calibrated with the 330-kOe field of α-Fe at ambient temperature.

2.3 Catalyst test

FTS performances over these supported catalysts were performed in a fixed-bed stainless steel reactor (6.0 mm inner diameter). Prior to reaction, the as-prepared catalysts (0.25 g) were *in situ* reduced at 400 °C for 10 h in a pure H_2 flow (40 mL min^{-1}). After reduction, the temperature was dropped to 320 °C. Subsequently, CO/H_2/Ar (32.0 vol% / 64.0 vol% / 4.0 vol%) reactant gas was introduced into the reactor, and the system was pressured gradually to 2.0 MPa. N-octane as solvent was equipped to capture the liquid hydrocarbons in the effluents. The obtained liquid hydrocarbons were analyzed by an off-line gas chromatograph (GC) using a flame ionization detector (FID). CO conversion, CO_2 selectivity, and hydrocarbons selectivity were calculated according to equation (1), (2), and (3), respectively.

$$\mathrm{CO}_{\text{conversion (\%)}} = \frac{\mathrm{CO_{in}} - \mathrm{CO_{out}}}{\mathrm{CO_{in}}} \times 100\% \quad (1)$$

CO_{in}: mole fraction of CO in the inlet, CO_{out}: mole fraction of CO in the outlet.

$$CO_2\ \text{selectivity}\ (\%) = \frac{CO_{2\ out}}{CO_{in} - CO_{out}} \times 100\% \quad (2)$$

CO_2 out: mole fraction of CO_2 in the outlet.

$$C_i\ \text{hydrocarbon selectivity}\ (C\text{-mol}\ \%) = \frac{\text{Mole of } C_i \text{ hydrocarbons} \times i}{\sum_{i=1}^{n} \text{Mole of } C_i \text{ hydrocarbons} \times i} \times 100\% \quad (3)$$

3. Results and Discussions

XRD patterns of G support and nitrogen regulated AG support were presented in Fig. 2.1. As seen, the characteristic diffraction peaks of support materials with the treatment of ammonia water were similar to that of parent support. Fig. 2.2 displayed XRD patterns of as-prepared catalysts as well as used catalysts. By contrast, although 5 wt% Fe elements were impregnated in support materials, no characteristic diffraction peaks ascribing to iron species appeared for Fe/G-W, Fe/AG-W, and Fe/AG-C catalysts (Fig. 2.1 and Fig. 2.2). Meanwhile, for these spent catalysts, no characteristic diffraction peaks associating with iron species were found after catalytic reactions. This phenomenon could be ascribed to the low content or well distribution of iron species (Table 2.1).

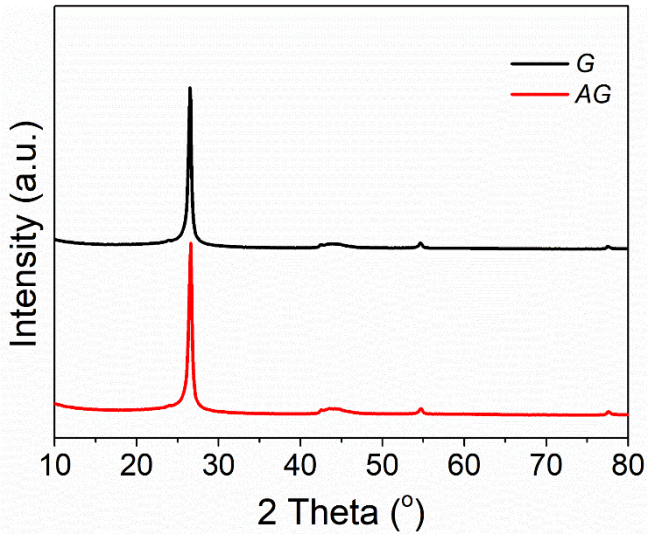

Fig. 2.1 XRD patterns of different graphene support materials.

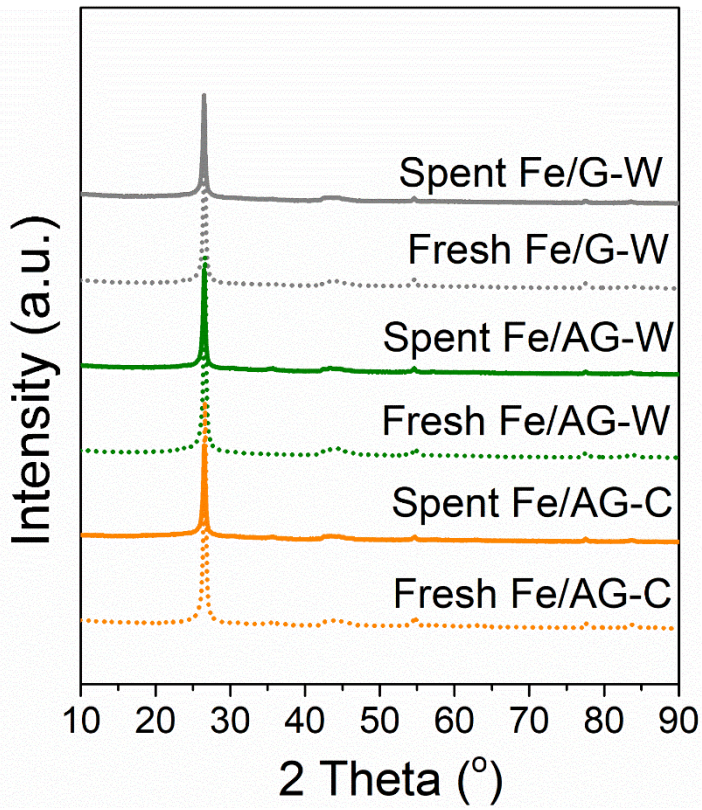

Fig. 2.2 XRD patterns of as-prepared and spent Fe/G-W, Fe/AG-W, and Fe/AG-C catalysts.

Table 2.1 Surface elemental compositions of different spent catalysts.

Catalyst	Element composition (at. %)	
	Fe	N
Fe/G-W	0.09	/
Fe/AG-W	0.05	0.35
Fe/AG-C	0.07	0.37

Catalyst surface characteristics is an important factor affecting the reaction performance, thus XPS was used to test the surface phase composition (Fig. 2.3). The binding energy peaks at 709, 711, and 714 eV in the Fe2p spectrum were ascribed to Fe-C, Fe^{II}, and Fe^{III}, respectively [27, 28]. To further reveal the presence of carbides, Mössbauer spectra (MES) of the spent catalysts were compared in Fig. 2.4 and Table 2.2. As seen, Fe_3C species was found in the spent catalysts [29]. Combined with XRD, XPS and MES, the results shown that the carbides could be uniformly dispersed on the surface of the catalyst. The N_2 physisorption results of G and AG were also compared in Fig. 2.5 and Table 2.3. Apparently, the surface areas of supports remained stable regardless of the nitrogen-containing group modification. With the following impregnation of iron species, the surface areas of different catalysts decreased clearly (Fig. 2.6 and Table 2.3). It should be noted that the catalysts with N modification presented a higher surface area than Fe/G-W such as Fe/AG-W and Fe/AG-C.

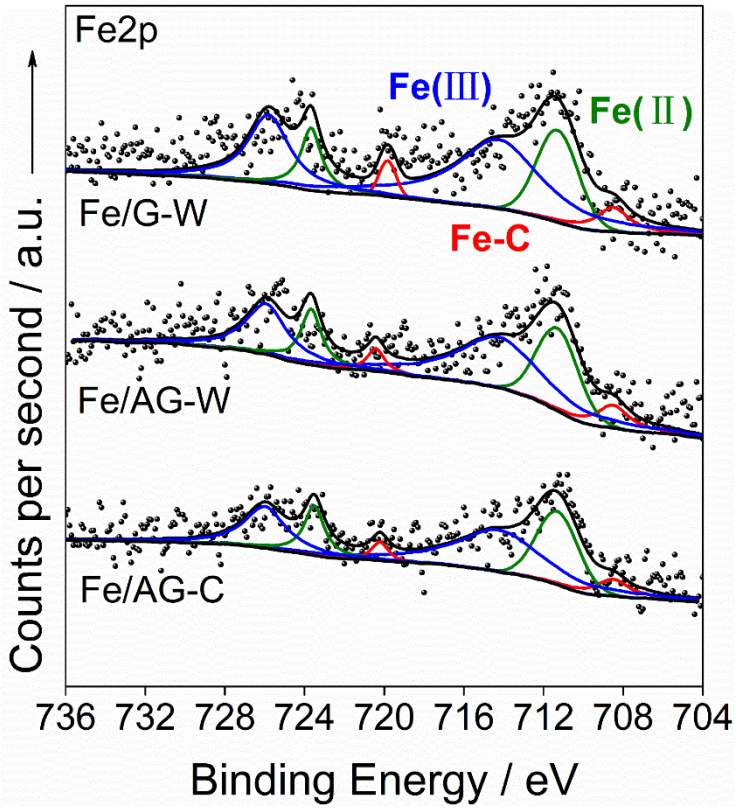

Fig. 2.3 Fe2p XPS spectra of spent Fe/G-W, Fe/AG-W, and Fe/AG-C.

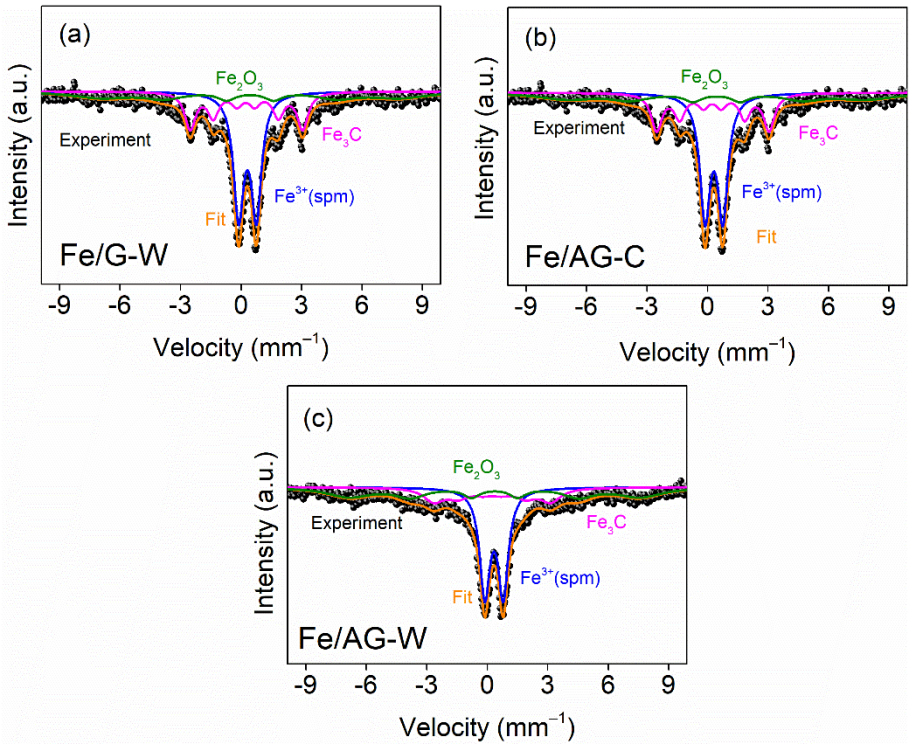

Fig. 2.4 [57] Fe Mössbauer spectra of various catalysts.

Table 2.2 Mössbauer spectra parameters obtained from different catalysts.

Catalysts	IS (mm/s)	QS (mm/s)	Hhf (kOe)	Phase
Fe/G-W	0.317	0.881	-	Fe^{3+}(spm)
	0.249	0.0312	-	θ-Fe_3C
	0.446	-	-	α-Fe_2O_3(Fe)
Fe/AG-W	0.334	0.914	-	Fe^{3+}(spm)
	0.241	0.0246	-	θ-Fe_3C
	0.362	-	-	α-Fe_2O_3(Fe)
Fe/AG-C	0.333	0.927	-	Fe^{3+}(spm)
	0.246	0.0582	-	θ-Fe_3C
	0.353	-	-	α-Fe_2O_3(Fe)

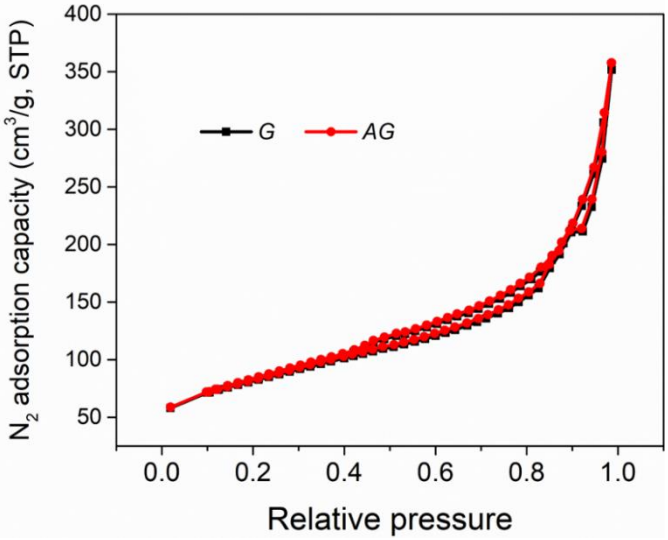

Fig. 2.5 N_2 adsorption-desorption isotherms of different graphene support materials.

Table 2.3 Surface areas of different catalysts.

Catalyst	Surface area (m^2/g)
G	278
AG	283
Fe/G-W	162
Fe/AG-W	179
Fe/AG-C	192

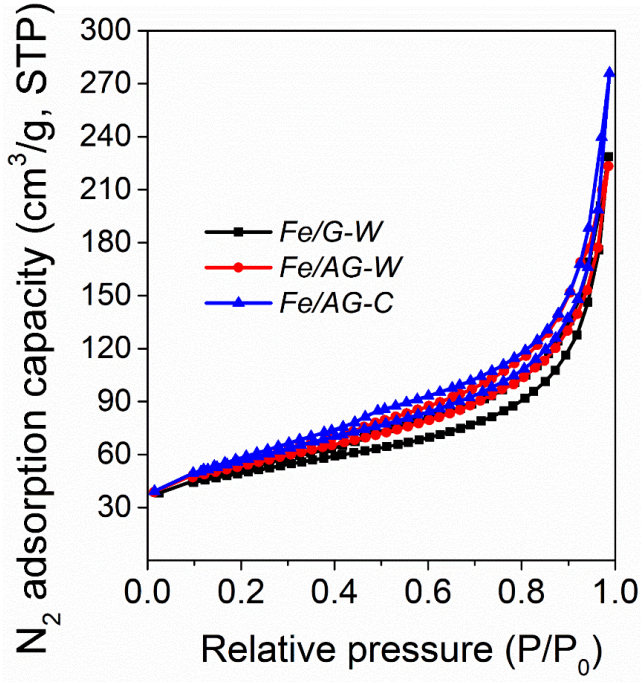

Fig. 2.6 N_2 adsorption-desorption isotherms of as-prepared Fe/G-W, Fe/AG-W, and Fe/AG-C.

C-C coupling is a structure-sensitive reaction, and the small-size particles have a profound influence on the catalytic activity and product selectivity [30]. Previously, Galvis et al. reported that the apparent TOF (surface-specific activity) increased 6–8 fold when the iron carbide size decreased from 7 to 2 nm [31]. Liu et al. found that the smaller iron carbides or iron species are beneficial to the formation of light olefins [32]. Similarly, Guo et al. also reported that the presence of small-size carbides are advantages in improving catalytic activity [33]. Correspondingly, TEM images were applied to compare the particle size or particle distribution (Fig. 2.7). As seen, for the Fe/G-W catalyst, the particle sizes were mainly concentrated in 50 nm. By contrast, compared to the particle sizes of Fe/G-W, the sizes of Fe/AG-W were rather small, mainly centered in 12 nm. Meanwhile, the particle

sizes of Fe/AG-C were similar to that of Fe/AG-W catalyst, exhibiting a rather small particle size. This suggested that microwave heating could not only quickly treat the catalyst (a few seconds rather than several hours), but also achieve heating purpose, just like the traditional calcination heating. Besides, it was clear that the iron species could be uniformly dispersed in smaller particles when the support was modified with nitrogen (Fig. 2.7).

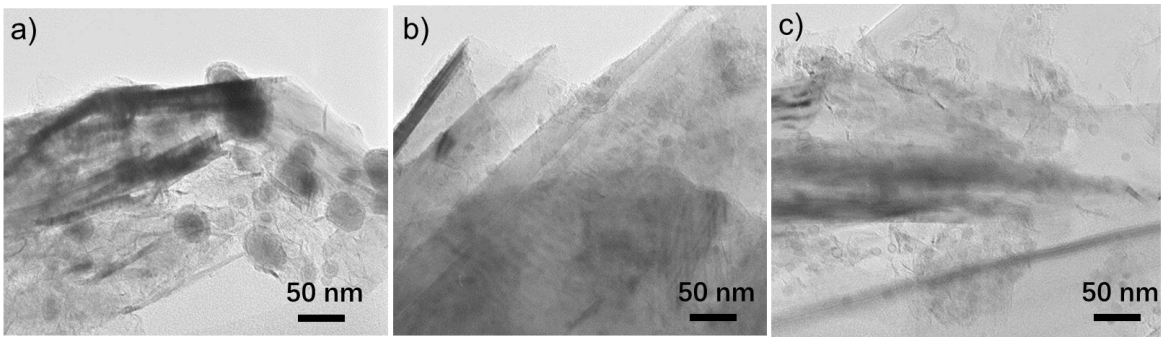

Fig. 2.7 (a) TEM images of spent Fe/G-W; (b) TEM images of spent Fe/AG-W; (c) TEM images of spent Fe/AG-C.

The surface reduction characteristics of catalysts can affect the reduction of metal oxides and the subsequent generation of active phases under reaction conditions. Based on this consideration, the surface reduction abilities of different catalysts were also investigated and compared. As drawn in Fig. 2.8, the peaks of Fe/C-W catalyst occurring between 300 ºC and 600 ºC could be attributed to the reduction of iron species [20, 34]. For the support with N modification supported iron catalyst treated by microwave heating, Fe/AG-W presented facile reduction processes. This indicated that nitrogen

modification was able to promote the reduction of Fe species (Fig. 2.8a, Fe/AG-W vs. Fe/G-W). Different from microwave heating (Fe/AG-W), although the low-temperature reduction region (300–400 °C) of the calcined Fe/AG-C catalyst increased, the high-temperature reduction region (400–500 °C) obviously decreased, suggesting that microwave treatment was more beneficial to the follow-up reduction of iron species. At the same time, the surface alkalinity of the catalyst was also studied (Fig. 2.8b). Peaks below 200 °C could be attributed to physical adsorption, while peaks above 400 °C were attributed to strong chemical adsorption. Obviously, the introduction of N enhanced the CO_2 adsorption in Fe/AG-C and Fe/AG-W, which is beneficial for CO_2 hydrogenation and conversion.

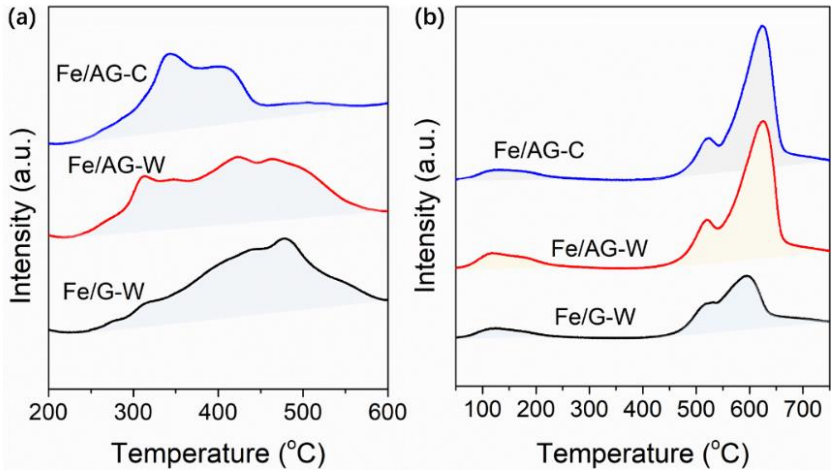

Fig. 2.8 (a) H_2-TPR and (b) CO_2-TPD profiles of the fresh Fe/G-W, Fe/AG-W, and Fe/AG-C catalysts.

The catalysts supported with different Fe loading were also characterized by XRD (Fig. 2.9). Different from 5%Fe/AG-W, the characteristic diffraction peaks ascribing to Fe_3O_4 (JCPDS 89–0691) appeared for the as-prepared catalysts with the increase of Fe loading [27]. After reaction, characteristic

diffraction peak associating to metallic iron species (JCPDS 06–0696) also appeared apart from Fe_3O_4 [27]. In addition, H_2-TPR profiles of different catalysts indicated that initial reduction temperature increases with the increase of Fe loading (Fig. 2.10). Considering that the appropriate metal loading had an important impact on improving the catalytic performance, the iron loading in the following research was controlled at 10%. As a rather convenient treatment method, microwave heating treatment could quickly synthesize the as-prepared catalyst, sharply shortening the synthesis cycles of catalysts. In this process, it was obvious that the length of microwave treatment time (heating temperature) can affect the characteristics of the final catalysts. Therefore, the effects of microwave heating time were investigated in detail.

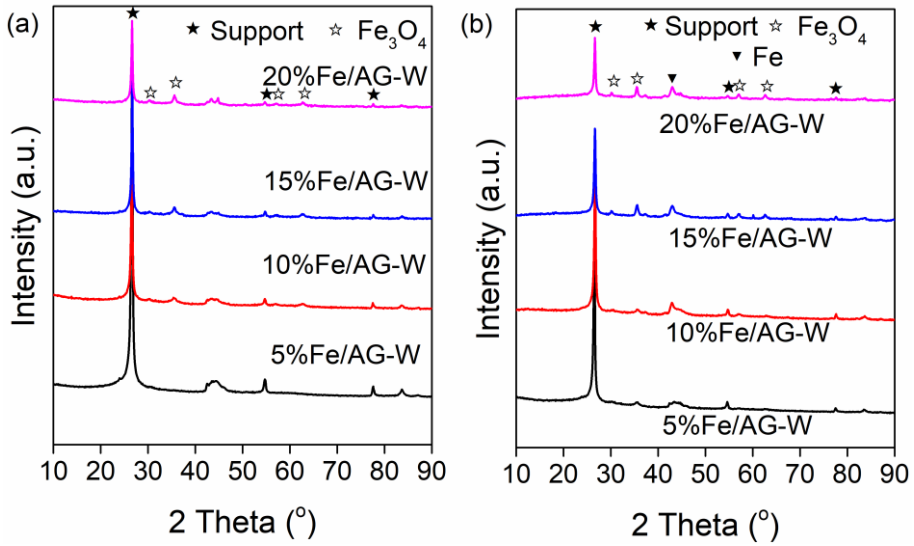

Fig. 2.9 XRD patterns of (a) as-prepared and (b) spent catalysts.

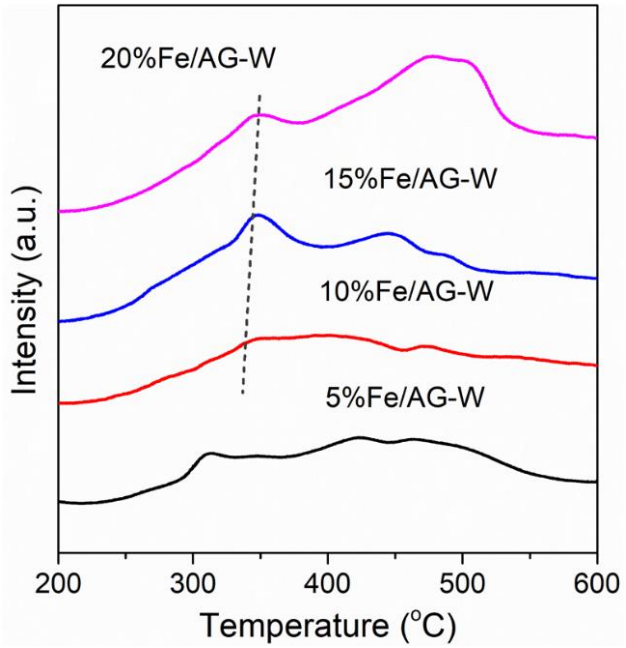

Fig. 2.10 H_2-TPR of the fresh 5%Fe/AG-W, 10%Fe/AG-W, 15%Fe/AG-W, 20%Fe/AG-W.

As depicted in Fig. 2.11 and Fig. 2.12, for the 10%Fe/AG-W(0), only characteristic peaks of the support material were present. However, after microwave heating treatment, the diffraction peaks of Fe_3O_4 appeared. When the characteristic diffraction peak of iron species appeared, further prolongation of microwave heating time not affected the final phase composition according to Fig. 2.11 (from 6 seconds to 18 seconds). For these spent catalysts, diffraction peak ascribed to metallic Fe appeared (Fig. 2.13). In addition, for the diffraction peak of metallic iron, the intensities of catalysts treated with microwave heating was greater than that without microwave heating, while the diffraction intensities of Fe_3O_4 exhibited an opposite trend. To some extent, the catalyst treated by microwave heating might be more beneficial to the formation of active phase.

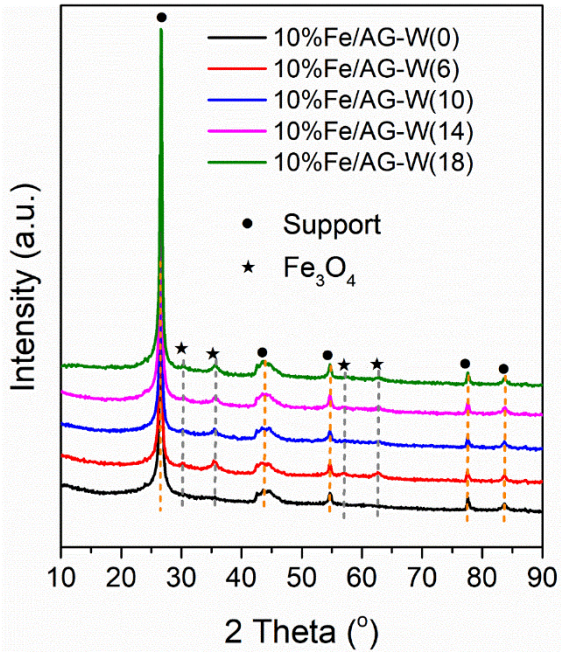

Fig. 2.11 XRD patterns of as-prepared catalysts.

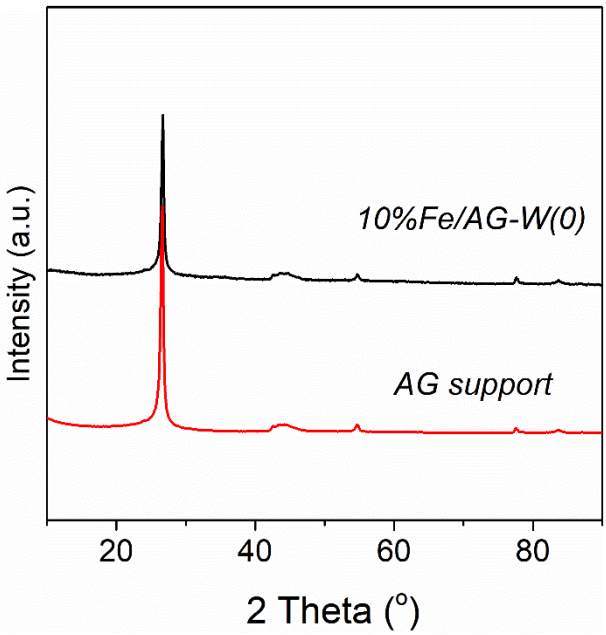

Fig. 2.12 XRD patterns of as-prepared 10%Fe/AG-W(0) and AG support.

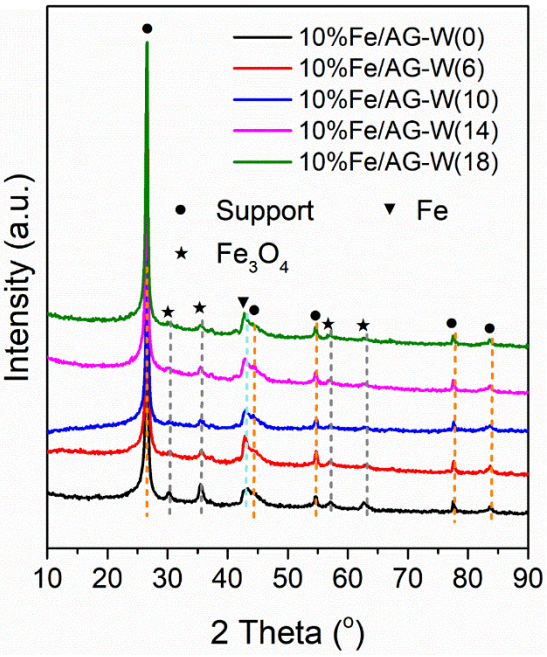

Fig. 2.13 XRD patterns of spent catalysts.

The reduction behaviors of various catalysts were compared in Fig. 2.14. Compared to 10%Fe/AG-W(0), 10%Fe/AG-W(6) exhibited a relatively lower reduction temperature. However, by further increasing the microwave heating time, the reduction temperature of iron species slightly became higher (Fig. 2.14). Fe2p XPS spectra of spent catalysts were drawn in Fig. 2.15. As seen, a fitting peak that binds to the Fe-C bond appeared for each catalyst. Moreover, the content of the Fe-C bond of microwave-treated catalyst was higher than that of the untreated 10%Fe/AG-W (0) catalyst, which was crucial for improving catalytic performance. N1s XPS spectra were deconvoluted and fitted with four components (Fig. 2.16). The binding energy peaks at around 398.3, 400.2, 401.5, and 403.3 eV were assigned to pyridinic-N, pyrrolic-N, quaternary-N, and oxidized-N, respectively [28, 35]. For these catalysts, pyrrolic-N was the main bonding configurations of nitrogen. When the heating

treatment time exceeded 10s, the content of pyridinic-N decreased significantly (Fig. 2.16). Surface elemental compositions of catalysts with various microwave time were compared in Table 2.4. As the microwave time increased, the surface contents of N and Fe showed a volcanic trend. The low surface content of iron should be due to carbon support capsulation during heating treatment.

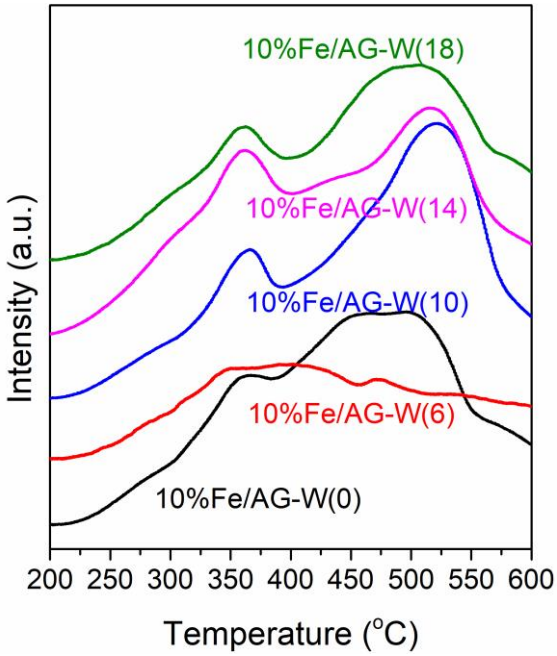

Fig. 2.14 H_2-TPR profiles of as-prepared catalysts.

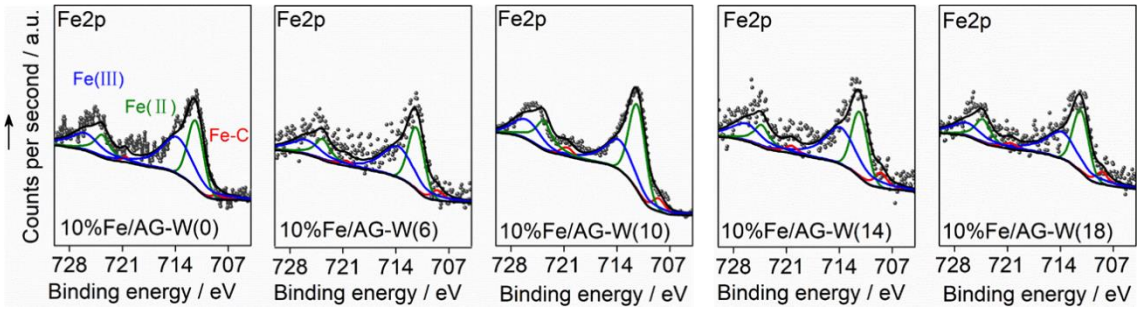

Fig. 2.15 Fe2p XPS spectra of spent 10%Fe/AG-W(0), 10%Fe/AG-W(6), 10%Fe/AG-W(10),

10%Fe/AG-W(14), and 10%Fe/AG-W(18) catalysts.

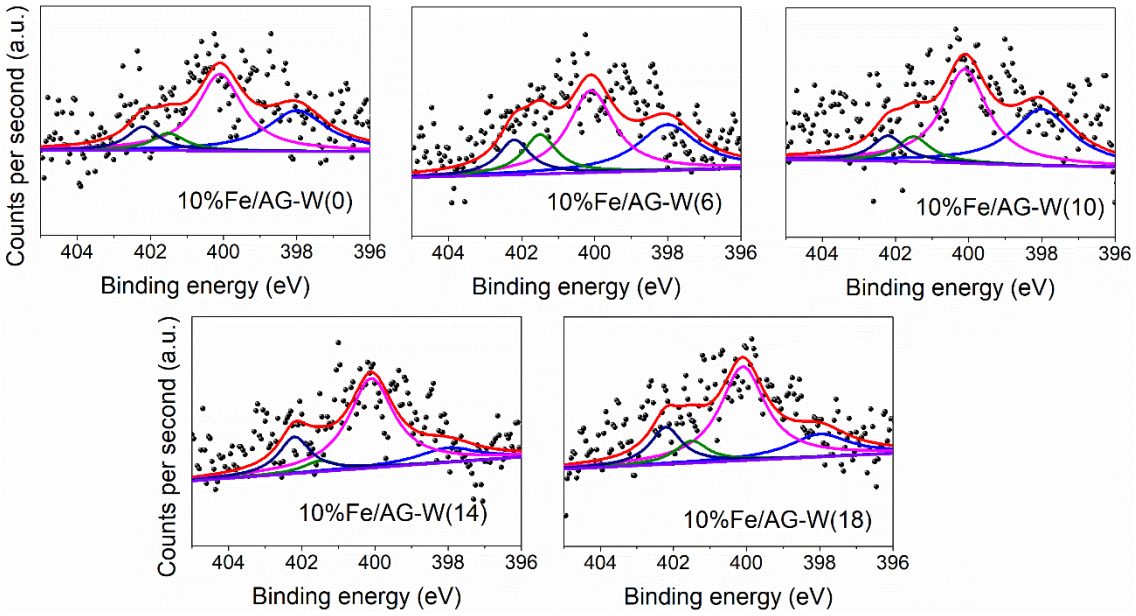

Fig. 2.16 High-resolution N1s XPS spectra of spent catalysts.

Table 2.4 Surface elemental compositions of different catalysts.

Catalyst	Element composition (at.%)	
	Fe	N
10%Fe/AG-W(0)	0.12	0.32
10%Fe/AG-W(6)	0.32	0.94
10%Fe/AG-W(10)	0.53	0.38
10%Fe/AG-W(14)	0.08	0.39
10%Fe/AG-W(18)	0.09	0.37

As mentioned above, chain propagation is a structure-sensitive reaction. As a consequence, particle size distributions of spent catalysts with various microwave times were compared in Fig. 2.17. For the 10%Fe/AG-W (0) catalyst without any heating treatment, the particle size was mainly

concentrated in about 120 nm. Different from 10%Fe/AG-W (0), the sizes were sharply reduced from 120 nm to 30 nm (10%Fe/AG-W (6)) with the utilization of heating treatment (6 seconds). When the microwave heat treatment time was prolonged (6–14 seconds), the particle size decreased further. But when the microwave treatment was extended to 18 seconds, the particle size began to increase again (10%Fe/AG-W (18)), which can be ascribed to the particle agglomeration at a high temperature [36]. It provided a facile manner for regulating particle size by controlling microwave time. More importantly, microwave treatment significantly shortened the heating time rather than conventional preparation processes.

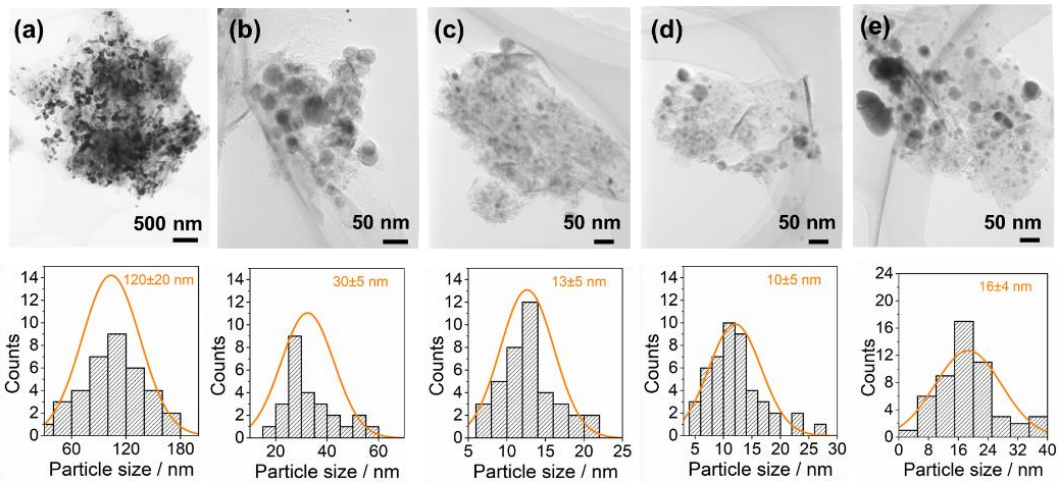

Fig. 2.17 TEM images of different spent catalysts and corresponding particle size distribution. (a) 10%Fe/AG-W(0); (b) 10%Fe/AG-W(6); (c) 10%Fe/AG-W(10); (d) 10%Fe/AG-W(14); (e) 10%Fe/AG-W(18).

In addition to studying the effect of microwave time on the physicochemical properties of the catalysts, the treatment time of graphene support with ammonium hydroxide was also investigated. As illustrated in Fig. 2.18a, for the as-prepared catalysts, the main phases were G support and Fe_3O_4. The prolongation of treatment time exhibited no effect on the phase composition of the as-prepared catalyst. For the spent catalysts (Fig. 2.18b), in addition to the characteristic diffraction peaks of the G support and Fe_3O_4, the characteristic peak of metallic Fe also appeared, and the spectra of different catalysts were similar to each other. H_2-TPR profiles reflected the reduction behavior of different catalysts (Fig. 2.18c). Reduction overlap peaks were observed for each catalyst, corresponding to the reductions of Fe_3O_4 species to metallic Fe. As presented in Fig. 2.18c, the reduction temperature of the Fe_3O_4 species was delayed with the extension of the $NH_3 \cdot H_2O$ treatment time for the graphene-supported iron nanoparticles. This indicated that the interaction between the metal iron species and the support became stronger with the increase of the $NH_3 \cdot H_2O$ treatment time. Meanwhile, the elemental compositions of different catalysts were concluded in Table 2.5. With the extension of $NH_3 \cdot H_2O$ treatment time, the content of N atoms (nitrogen-containing groups) in the support gradually increased, which was consistent with H_2-TPR results to some extent.

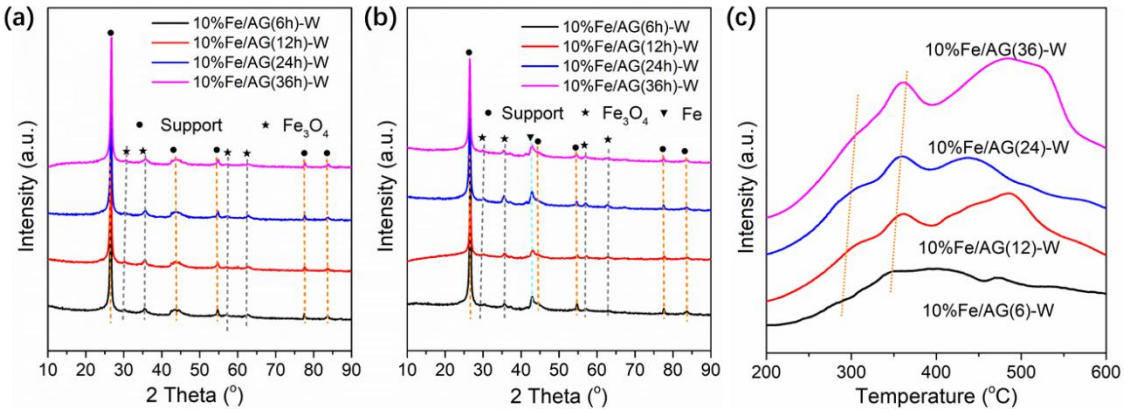

Fig. 2.18 (a)XRD patterns of as-prepared and (b) spent catalysts; (c) H_2-TPR profiles of the fresh 10%Fe/AG(6h)-W, 10%Fe/AG(12h)-W, 10%Fe/AG(24h)-W, 10%Fe/AG(36h)-W.

Table 2.5 Surface atom compositions of different catalysts.

Catalyst	Element composition (at.%)				% [a]	at.% [b]
	Fe	N	C	O		
10%Fe/AG(6h)-W	0.32	0.94	92.94	5.08	71	0.67
10%Fe/AG(12h)-W	0.18	1.23	93.86	4.73	63	0.77
10%Fe/AG(24h)-W	0.33	1.92	90.54	7.20	56	1.10
10%Fe/AG(36h)-W	0.37	2.99	90.00	6.64	31	0.93

Note: % [a] stands for the content of pyridinic-N and pyrrolic-N among four N configurations; at. % [b] stands for the N atoms content ascribing to pyridinic-N and pyrrolic-N.

Fe2p XPS spectra were deconvoluted and shown in Fig. 2.19. Three fitting peaks, corresponding to Fe^{III}, Fe^{II} and Fe–C, appeared in the spectra, which demonstrated the existence of active carbides. With the increase of nitrogen-containing groups, the content of carbides increased (Fig. 2.19a, Fig.

2.19b and Table 2.6). However, with the further increase of nitrogen content, the content of carbides decreased (Fig. 2.19c and Fig. 2.19d). These findings indicated that an appropriate amount of nitrogen-containing groups in support materials can improve the carbonization process and form more active sites, which was beneficial for the catalytic performance. Meanwhile, N1s XPS spectra of these nitrogen tailored catalysts were deconvoluted to determine the nitrogenous specie configurations (Fig. 2.19e–h). For the N1s spectrum of 10%Fe/AG (6h)-W catalyst, the binding energy peaks at around 398.3, 400.2, 401.5, and 403.3 eV were ascribed to pyridinic-N, pyrrolic-N, quaternary-N, and oxidized-N, respectively. And the main configurations of nitrogen species were pyridinic-N and pyrrolic-N (Fig. 2.19e). However, for 10%Fe/AG (12h)-W, the content of quaternary-N increased while the content of pyridinic-N decreased (Fig. 2.19f). Further increasing the treatment time of $NH_3 \cdot H_2O$, the configurations of N types changed, in which the contents of quaternary-N and oxidized-N increased and the content of pyridinic-N further decreased (Fig. 2.19g). More obviously, when the G support was treated with $NH_3 \cdot H_2O$ for up to 36 hours, the spectrum changed visibly. Different from 10%Fe/AG (6h)-W catalyst, the main configurations of nitrogen species were quaternary-N and oxidized-N. At the same time, the contents of pyridinic-N and pyrrolic-N decreased significantly, especially pyridinic-N. It could be concluded that the extension of $NH_3 \cdot H_2O$ treatment time can not only increase the content of N-atom but also change the configuration of nitrogen-containing species.

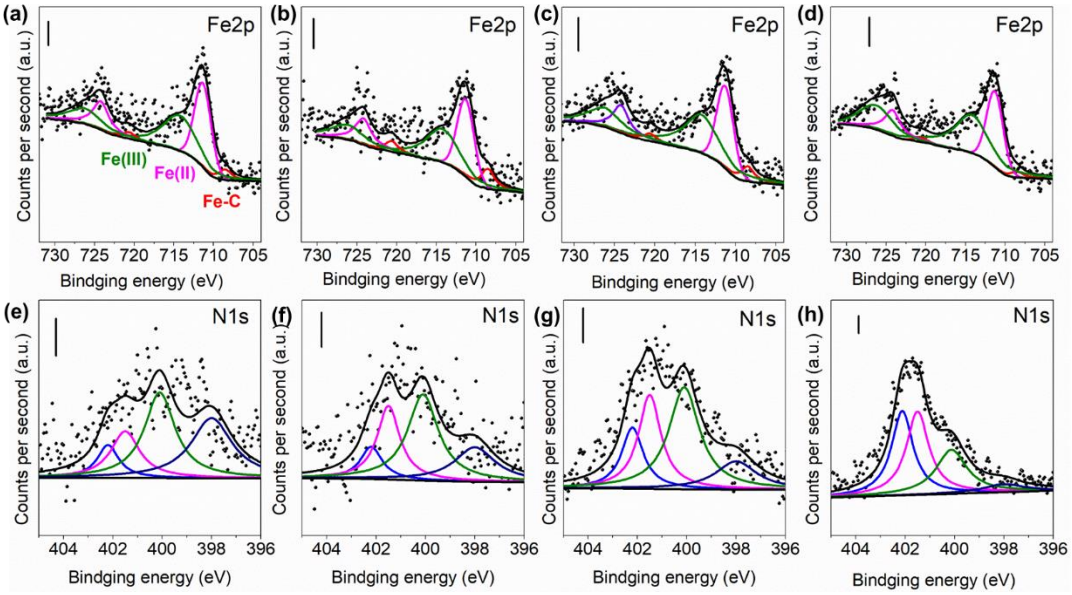

Fig. 2.19 Fe2p XPS spectra of (a) 10%Fe/AG (6h)–W, (b) 10%Fe/AG (12h)–W, (c) 10%Fe/AG (24h)–W, (d) 10%Fe/AG (36h)–W; N1s XPS spectra of (e) 10%Fe/AG (6h)–W, (f) 10%Fe/AG (12h)–W, (g) 10%Fe/AG (24h)–W, (h) 10%Fe/AG (36h)–W. The black bars in the images stand for 100 counts.

Table 2.6 Surface atom compositions of different catalysts.

Catalyst	Element composition (at.%)				% [a]	at.% [b]
	Fe	N	C	O		
10%Fe/AG(6h)-W	0.32	0.94	92.94	5.08	71	0.67
10%Fe/AG(12h)-W	0.18	1.23	93.86	4.73	63	0.77
10%Fe/AG(24h)-W	0.33	1.92	90.54	7.20	56	1.10
10%Fe/AG(36h)-W	0.37	2.99	90.00	6.64	31	0.93

Note: % [a] stands for the content of pyridinic-N and pyrrolic-N among four N configurations; at.% [b] stands for the N atoms content ascribing to pyridinic-N and pyrrolic-N.

Catalytic performances of FTS over graphene supported iron nanoparticles were obtained (Fig.

2.20). For Fe/G-W catalyst, the CO conversion was about 72% and CO_2 selectivity was 35% under the reaction conditions (320 ºC, W/F = 5 g h mol^{-1}, P = 2.0 MPa). C_5^+ selectivity approached 17.1% among whole hydrocarbons. With the incorporation of N-atoms, CO conversion increased visibly (85% conversion for Fe/AG-W) although CO_2 selectivity increased slightly. Besides, C_{5+} selectivity increased from 17.1% to 23.2%. For Fe/AG-C catalyst, CO conversion was slightly worse than that of Fe/AG-W. It indicated that microwave treatment was also a benign and rather fast heating process. As characterized, with the nitrogen modification, iron species presented a rather small size (Fig. 2.7). Previously, Pour et al. reported that CO conversion increased with the decrease of iron species size [37, 38]. Lama et al. also reported that a nitrogen-doped carbon layer stabilized atomically small Fe species, and could enable much faster activation of the Fe species [39]. To some extent, H_2-TPR profiles also reflected that nitrogen-modified Fe-based catalysts were more conducive to the activation and generation of active sites (Fig. 2.8). It was reasonable to infer that the introduction of N-atoms apparently promoted the formation of small-size particles of iron species, which was conducive to improve FTS performance. Besides, the existences of nitrogen-containing groups could effectively suppress the methane selectivity and improve the olefins selectivity (Fig. 2.20), which had been reported by Liu et al [20].

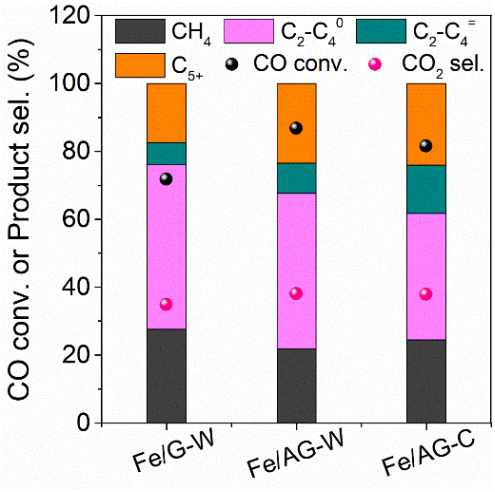

Fig. 2.20 Catalytic activity and product selectivity over three kinds of graphene supported iron catalyst. Reaction conditions: 320 °C, W/F = 5 g h mol^{-1}; P = 2.0 MPa.

Catalytic performances of FTS over iron-based catalysts with various iron loading were compared in Fig. 2.21. When the iron loading increased from 5% to 10%, FTS performance was significantly improved, and the conversion increased from 85% to more than 97%, and the selectivity of by-product CO decreased. Apart from that, heavy hydrocarbon selectivity also increased (Fig. 2.21). Based on this consideration, the influences of different microwave treatment time on the catalytic performance were shown in Fig. 2.22. For the 10%Fe/AG-W (0) without any heating pretreatment, CO conversion was about 82%. By contrast, with the microwave heating treatment, CO conversion was increased to 98% for 10%Fe/AG-W (6). Further increasing heating treatment time, CO conversion remained above 96%. When the microwave treatment time was 10s, it showed a conversion of 96.3%, with the selectivity of 28.8% for CO and 36.1% for C_{5+} hydrocarbons. These results indicated that facile microwave heating

could significantly promote the improvement of FTS performance. As shown in Fig. 2.11, with the heating treatment, Fe_3O_4 phases of as-prepared catalysts appeared instead of 10%Fe/AG-W (0). On the contrary, after reaction, Fe_3O_4 phase was more favorable to be converted into metallic iron, thus promoting the formation of the active phase (Fig. 2.22). As the active sites for chain coupling, more carbides were conducive to promote FTS performance (Fig. 2.22) [40, 41]. More importantly, with the utilization of rapid microwave heating, more small-size carbides were formed compared with 10%Fe/AG-W (0) (Fig. 2.17). As a consequence, the small-size carbides species played crucial roles for improving catalytic performance.

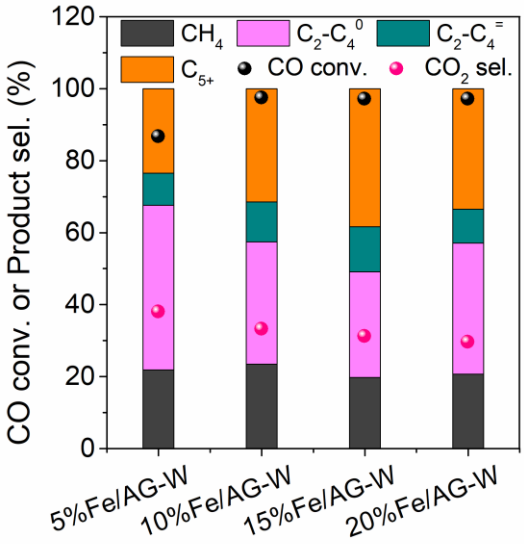

Fig. 2.21 Catalytic activity and product selectivity. Reaction conditions: 320 °C, W/F = 5 g mol^{-1} h^{-1}; P = 2.0 MPa.

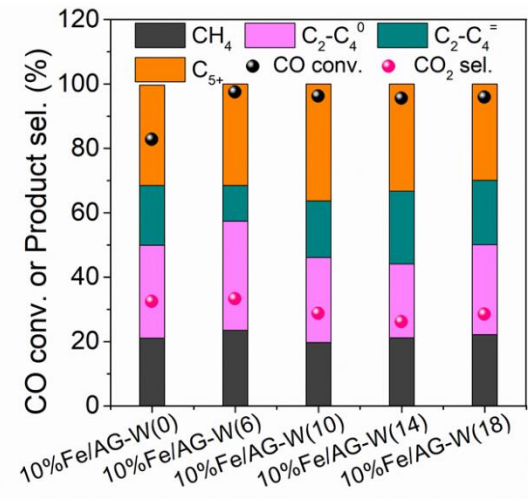

Fig. 2.22 Catalytic activity and product selectivity over different graphene-supported iron catalysts with various microwave treatment time. (a) Effects of iron content on catalytic performance. Reaction conditions: 320 °C, W/F = 5 g h mol^{-1}; P = 2.0 MPa.

Catalytic performances of FTS over iron-based catalysts with different $NH_3 \cdot H_2O$ treatment time were also compared in Fig. 2.23. For these catalysts, CO conversion did not depend on the length of $NH_3 \cdot H_2O$ treatment, and the conversion remained above 96%. However, olefin secondary hydrogenation abilities over these catalysts were different. The alkenes selectivity increased when the $NH_3 \cdot H_2O$ treatment time was 12 hours, indicating the weak hydrogenation ability than 10%Fe/AG (6)-W. In addition, with the extension of treatment time, although the configurations of pyridinic-N and pyrrolic-N decreased significantly (Fig. 2.19), the surface relative contents of pyridinic-N and pyrrolic-N also increased (Table 2.6). Meanwhile, the content of carbides also increased (Fig. 2.19). Previously, it is reported that pyridinic-N and pyrrolic-N atoms played a crucial role in binding the Fe atoms while

quaternary-N atoms play a minor role [42]. Metal species generally tended to attach to the defect sites, and these nitrogen-containing configurations might lead to the generation of vacancies or other defects in the graphitic lattice [43, 44]. Thus, high alkene-rich hydrocarbons could be ascribed to the metal-like promoter modification (pyridinic-N and pyrrolic-N). Besides, compared to the FTS performance over conventional iron-based catalysts, CO conversion as well as product selectivity here presented superior values over the reported literatures. More importantly, through the rapid heating treatment, the fabrication of an efficient iron nanoparticles catalyst could remarkably shorten the preparation cycle, which had a good meaning for practical industry.

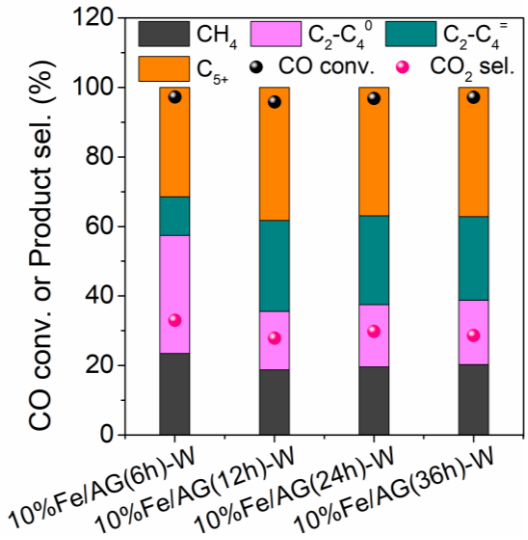

Fig. 2.23 Catalytic activity and product selectivity. Effects of ammonia water treatment time on catalytic performance. Reaction conditions: 320 °C, W/F = 5 g h mol^{-1}; P = 2.0 MPa.

4. Conclusions

Nitrogen-regulated graphene supported iron nanoparticles assisted by microwave treatment were successfully prepared for Fischer-Tropsch synthesis. Different from conventional calcination processes, fast microwave treatment achieved a good heating process. Nitrogen modification of supports was able to effectively anchor iron species, promote the uniform distribution of small-size iron species and then promote catalytic activity. Moreover, the particle size of the supported iron species (from 120 nm to 10 nm) was effectively regulated by adjusting the microwave heating time. Besides, with the extension of $NH_3 \cdot H_2O$ treatment time, the contents of N-containing groups increased and the types of N configuration changed significantly. Proper treatment time helped to increase the contents of available N configuration, promoting the formation of alkene-rich hydrocarbons. The obtained catalyst presented ultra-high CO conversion and benign product selectivity under relevant industrial conditions. Thus, this design of graphene supported iron nanoparticles with the utilization of rapid heating treatment provides a new strategy for FTS to produce high value-added products (heavy hydrocarbons), and sheds a light on the rational design of high efficiently catalysts for practical industry in the future.

References

(1) Li, J et al. Integrated tuneable synthesis of liquid fuels via Fischer-Tropsch technology. *Nat Catal*. **1**, 787–793 (2018).

(2) Peron, D.V. et al. Active phases for high temperature Fischer-Tropsch synthesis in the silica supported iron catalysts promoted with antimony and tin. *Appl Catal B-Environ*. **292**, 120141 (2021).

(3) Bae, J.-S. et al. Eco-friendly prepared iron-ore-based catalysts for Fischer-Tropsch synthesis. *Appl Catal B-Environ*. **244**, 576–582 (2019).

(4) Xu, Y. et al. A hydrophobic FeMn@Si catalyst increases olefins from syngas by suppressing C1 by-products. *Science*. **371**, 610–613 (2021).

(5) Chen, Y. et al. Preparation of SiO_2 immobilized Co-based catalysts from ZIF-67 and the enhancement effect for Fischer-Tropsch synthesi. *Appl Catal B-Environ*. **289**, 120027 (2021).

(6) Sun, B. et al. One-Pot Approach to a Highly Robust Iron Oxide/Reduced Graphene Oxide Nanocatalyst for Fischer-Tropsch Synthesis. *ChemCatChem*. **5**, 714–719 (2013).

(7) Xiong, H. et al. Shaped Carbons As Supports for the Catalytic Conversion of Syngas to Clean Fuels. *ACS Catal*. **5**, 2640–2658 (2015).

(8) Chen, Q. et al. Design of ultra-active iron-based Fischer-Tropsch synthesis catalysts over spherical mesoporous carbon with developed porosity. *Chem Eng J*. **334**, 714–724 (2018).

(9) Zhao, H. et al. Iron oxide nanoparticles supported on pyrolytic graphene oxide as model catalysts for Fischer Tropsch synthesis. *Appl Catal A-Gen*. **456**, 233–239 (2013).

(10) Wei, Y. et al. Mesoporous Iron Oxide Nanoparticle-Decorated Graphene Oxide Catalysts for Fischer–Tropsch Synthesis. *ACS Appl Nano Mater*. **3**, 7182–7191 (2020).

(11) Moussa, S.O. et al. L.S. Graphene-Supported Iron-Based Nanoparticles for Catalytic Production of Liquid Hydrocarbons from Synthesis Gas: The Role of the Graphene Support in Comparison with Carbon Nanotubes. *ACS Catal*. **4**, 535–545 (2014).

(12) Wang, C. et al. Synthesis of Highly Stable Graphene-Encapsulated Iron Nanoparticles for Catalytic Syngas Conversion. *Part Part Syst Char*. **32**, 29–34 (2015).

(13) Wei, Y. et al. Enhanced Fischer–Tropsch performances of graphene oxide-supported iron catalysts via argon pretreatment. *Catal Sci Technol*. **8**, 1113–1125 (2018).

(14) Tian, Z. et al. Fischer-Tropsch synthesis to light olefins over iron-based catalysts supported on $KMnO_4$ modified activated carbon by a facile method. *Appl Catal A-Gen*. **541**, 50–59 (2017).

(15) Luk, H.T. et al. Role of Carbonaceous Supports and Potassium Promoter on Higher Alcohols Synthesis over Copper–Iron Catalysts. *ACS Catal*. **8**, 9604–9618 (2018).

(16) Cheng, Y. et al. Potassium-promoted magnesium ferrite on 3D porous graphene as highly efficient catalyst for CO hydrogenation to lower olefins. *J Catal*. **374**, 24–35 (2019).

(17) Zhai, P. et al. Highly tunable selectivity for syngas-derived alkenes over Zinc and Sodium-modulated Fe_5C_2 catalyst. *Angew Chem Int Ed*. **55**, 1–7 (2016).

(18) Liu, Y. et al. Manganese-Modified Fe_3O_4 Microsphere Catalyst with Effective Active Phase of Forming Light Olefins from Syngas. *ACS Catal*. **5**, 3905–3909 (2015).

(19) Li, Z. et al. Enhanced Fischer-Tropsch synthesis performance of iron-based catalysts supported on nitric acid treated N-doped CNTs. *Appl Surf Sci*. **347**, 643–650 (2015).

(20) Liu, G. et al. Nitrogen-rich mesoporous carbon supported iron catalyst with superior activity for Fischer-Tropsch synthesis. *Carbon*. **130**, 304–314 (2018).

(21) Xiong, H. Fischer–Tropsch synthesis: Iron-based catalysts supported on nitrogen-doped carbon nanotubes synthesized by post-doping. *Appl Catal A-Gen*. **482**, 377–386 (2014).

(22) Lee, J.H. et al. Phase-controlled synthesis of thermally stable nitrogen-doped carbon supported iron catalysts for highly efficient Fischer-Tropsch synthesis. *Nano Res*. **12**, 2568–2575 (2019).

(23) Schulte, H.J. et al. Nitrogen- and Oxygen-Functionalized Multiwalled Carbon Nanotubes Used as Support in Iron-Catalyzed, HighTemperature Fischer-Tropsch Synthesis. *ChemCatChem*. **4**, 350–355 (2012).

(24) Lu, J. et al. Promotion Effects of Nitrogen Doping into Carbon Nanotubes on Supported Iron Fischer–Tropsch Catalysts for Lower Olefins. *ACS Catal.* **4**, 613–621 (2014).

(25) Tang, L. et al. Iron-based catalysts encapsulated by nitrogen-doped graphitic carbon for selective synthesis of liquid fuels through the Fischer-Tropsch process. *Chinese J Catal*. **39**, 1971–1979 (2018).

(26) Chen, X. et al. N-doped graphene as an electron donor of iron catalysts for CO hydrogenation to light olefins. *Chem Commun*. **51**, 217–220 (2015).

(27) Guo, L. et al. Directly converting carbon dioxide to linear α-olefins on bio-promoted catalysts. *Commun Chem*. **1**, 11 (2018).

(28) Zeng, Z. et al. Hierarchically porous carbon with pentagon defects as highly efficient catalyst for oxygen reduction and oxygen evolution reactions. *J Mater Sci*. **55**, 4780–4791 (2020).

(29) Pérez-Alonso, F.J. et al. Evolution of the bulk structure and surface species on Fe–Ce catalysts during the Fischer–Tropsch synthesis. *Green Chem*. **9**, 663–670 (2007).

(30) Liu, J. et al. Particle Size and Crystal Phase Effects in Fischer-Tropsch Catalysts. *Engineering*. **3,** 467–476 (2017).

(31) Galvis, H.M.T. et al. Iron particle size effects for direct production of lower olefins from synthesis gas. *J Am Chem Soc*. **134**, 16207–16215 (2012).

(32) Liu, Y. et al. The effect of pore size or iron particle size on the formation of light olefins in Fischer–Tropsch synthesis. *RSC Adv*. **5**, 29002–29007 (2015).

(33) Guo, L. et al. Spinel-structure catalyst catalyzing CO_2 hydrogenation to full spectrum alkenes with an ultra-high yield. *Chem Comm*. **56**, 9372–9375 (2020).

(34) Wei, J. et al. New insights into the effect of sodium on Fe_3O_4-based nanocatalysts for CO_2 hydrogenation to light olefins. *Catal Sci Technol*. **6**, 4786–4793 (2016).

(35) Gorgulho, H.F. et al. Synthesis and characterization of nitrogen-doped carbon xerogels. *Carbon*. **47**, 2032–2039 (2009).

(36) Goodman, E.D. et al. Mechanistic Understanding and the Rational Design of Sinter-Resistant Heterogeneous Catalysts. *ACS Catal*. **7**, 7156–7173 (2017).

(37) Pour, A.N. et al. Size-dependent studies of Fischer–Tropsch synthesis on iron based catalyst: New

kinetic model. *Fuel*. **116**, 787–793 (2014).

(38) Pour, A.N. et al. Fischer-Tropsch synthesis by nano-structured iron catalyst. *J Nat Gas Chem*. **19,** 284–292 (2010).

(39) Lama, S.M.G. et al. Tandem promotion of iron catalysts by sodium-sulfur and nitrogen-doped carbon layers on carbon nanotube supports for the Fischer-Tropsch to olefins synthesis. *Appl Catal A-Gen*. **568**, 213–220 (2018).

(40) Ma, C. et al. θ-Fe3C dominated Fe@C core–shell catalysts for Fischer-Tropsch synthesis: Roles of θ-Fe_3C and carbon shell. *J Catal.* **393**, 238–246 (2021).

(41) Qiu, T. et al. SAPO-34 zeolite encapsulated Fe_3C nanoparticles as highly selective Fischer-Tropsch catalysts for the production of light olefins. *Fuel*. **203**, 811–816 (2017).

(42) Xiong, H. et al. Fischer–Tropsch synthesis: Iron catalysts supported on N-doped carbon spheres prepared by chemical vapor deposition and hydrothermal approaches. *J Catal*. **311,** 80–87 (2014).

(43) Guo, L. et al. One-Pot Hydrothermal Synthesis of Nitrogen Functionalized Carbonaceous Material Catalysts with Embedded Iron Nanoparticles for CO_2 Hydrogenation. *ACS Sustainable Chem Eng*. **7,** 8331–8339 (2019).

(44) He, L. et al. Synthesis, Characterization, and Application of Metal Nanoparticles Supported on Nitrogen-Doped Carbon: Catalysis beyond Electrochemistry. *Angew Chem Int Ed*. **55**, 12582–12594 (2016).

Summary

With the combustion of fossil fuels for industrialization and transportation, large amount of CO_2 and CO were released into the air atmosphere. Therefore, the question of dealing with the CO_2 and CO are getting more and more attention. Meanwhile, considering the target of sustainable development, a feasible and promising solution for long-term sustainable development is the highly selective catalysis of CO_2 and CO into valuable chemicals, such as aromatics and heavy hydrocarbons (C_5^+).

In this paper, we first converted the greenhouse gas CO_2 into aromatics (chapter 1), which are chemicals used to produce industrial products. Composite catalysts containing a K-Fe-Zn catalyst and a NaOH-treated ZSM-5 zeolite were utilized. The bifunctional catalysts achieved the processes of CO_2 to light olefins and light olefins to aromatics, where the bimetallic catalyst was responsible for the light olefin production and the ZSM-5 zeolite was responsible for the aromatization of light olefins, respectively.

We also investigated the influence of the ratios of Fe/Zn, the ratios of SiO_2/Al_2O_3, the concentrations of NaOH solutions, and the weight ratios of K-Fe-Zn to ZSM-5. The results showed that when the ratio of Fe/Zn was 3, the catalyst exhibited the highest light olefin selectivity, which were important intermediates in the following aromatization process. Besides, when the SiO_2/Al_2O_3 was 21, the concentration of NaOH was 0.2 M, and the weight ratio was 1:3, the composite catalyst

presented the best aromatic selectivity, which indicated the best light olefin transport and conversion efficiency.

In summary, in chapter 1, an efficient composite catalyst could be rationally constructed by regulating component composition and the microenvironment of zeolite for directly converting CO_2 into aromatics.

In chapter 2, we successfully converted CO gas into heavy hydrocarbons (C_5^+ hydrocarbons) via a nitrogen-regulated graphene-supported Fe nanoparticle catalyst. We explored the influence of the Fe content, the heating time, and the solution time of $NH_3 \cdot H_2O$. We found that when the Fe content was 15%, the heating time was 10 seconds, and the solution time was 10 hours, the optimized 15%Fe/AG(12 h)-W(10) achieved the CO conversion of 97.2% and C_5^+ selectivity of 40.0%, while the by-product CO_2 selectivity was only 28.2%.

Furthermore, this work proposed the new concept of quick microwave assembling, which utilized a microwave rather than a muffle furnace during the heating process. The new method greatly decreased the heating time (from several hours to several seconds) and exhibited better catalytic performance and C_5^+ selectivity. A lot of excellent absorbents of microwaves, like graphene, here act as benign support materials, and consequently the microwave-assisted method sheds a light on the general design of high efficiently supported catalysts (not limited to Fe-based catalysts) for practical industry in future.

In conclusion, direct synthesis of aromatics and C_5^+ hydrocarbons from CO_2 and CO was successfully achieved via tailor-made catalysts and exhibited well performances. We believed that the findings of these works can provide useful knowledge and offer valuable guidance for designing other efficient catalysts for CO_2/CO conversion.

List of publications

(1) **Jiaming Liang**, Jiangtao Liu, Lisheng Guo, Wenhang Wang, Chengwei Wang, Weizhe Gao, Xiaoyu Guo, Yingluo He, Guohui Yang, Shuhei Yasuda, Bing Liang, Noritatsu Tsubaki. CO_2 hydrogenation over Fe-Co bimetallic catalysts with tunable selectivity through a graphene fencing approach. *Nature Communications.* **15**, 512 (2024).

(2) **Jiaming Liang**, Lisheng Guo, Weizhe Gao, Chengwei Wang, Xiaoyu Guo, Yingluo He, Guohui Yang, Noritatsu Tsubaki. Direct conversion of CO_2 to aromatics over K-Zn-Fe/ZSM-5 catalysts via a Fischer-Tropsch synthesis pathway. *Industrial & Engineering Chemistry Research*. **61**, 10336–10346 (2022). **(Chapter 1)**

(3) Lisheng Guo, Zhongshan Guo, **Jiaming Liang**, Xiaojing Yong, Song Sun, Wei Zhang, Jian Sun, Tiejian Zhao, Jie Li, Yu Cui, Baizhang Zhang, Guohui Yang, Noritatsu Tsubaki. Quick Microwave Assembling Nitrogen-Regulated graphene supported iron nanoparticles for Fischer-Tropsch synthesis. *Chemical Engineering Journal*. **429**, 132063 (2022). **(Chapter 2)**

(4) Yingluo He, **Jiaming Liang**, Yusuke Imai, Koki Ueda, Hangjie Li, Xiaoyu Guo, Guohui Yang, Yoshiharu Yoneyama, Noritatsu Tsubaki. Highly selective synthesis of methanol from methane over carbon materials supported Pd-Au nanoparticles under mild conditions. *Catalysis Today*. **352**, 104–110 (2020).

(5) Kangzhou Wang, Xiaobo Peng, Xinhua Gao, Yuya Araki, Heng Zhao, **Jiaming Liang**, Liwei Xiao,

Jienan Chen, Guangbo Liu, Jinhu Wu, Guohui Yang, Noritatsu Tsubaki. Insights into the synergistic effect of active centers over ZnMg/SBA-15 catalysts in direct synthesis of butadiene from ethanol. *Reaction Chemistry & Engineering*. **6**, 548–558 (2021).

(6) Yan Zeng, Ayano Kimura, Peipei Zhang, **Jiaming Liang**, Jiaqi Fan, Liwei Xiao, Chengwei Wang, Guohui Yang, Xiaobo Peng, Noritatsu Tsubaki. Resistance against carbon deposition via controlling spatial distance of catalytic components in methane dehydroaromatization. *Catalysts*. **11**, 148 (2021).

(7) Fei Chen, Peipei Zhang, Liwei Xiao, **Jiaming Liang**, Baizhang Zhang, Heng Zhao, Rungtiwa Kosol, Qingxiang Ma, Jienan Chen, Xiaobo Peng, Guohui Yang, Noritatsu Tsubaki. Structure-Performance Correlations over Cu/ZnO interface for low-temperature methanol synthesis from syngas containing CO_2. *ACS Applied Materials & Interfaces*. **13**, 8191–8205 (2021).

(8) Minghui Tan, Sha Tian, Tao Zhang, Kangzhou Wang, Liwei Xiao, **Jiaming Liang**, Qingxiang Ma, Guohui Yang, Noritatsu Tsubaki, Yisheng Tan. Probing hydrophobization of a Cu/ZnO catalyst for suppression of water-gas shift reaction in syngas conversion. *ACS Catalysis*. **11**, 4633–43 (2021).

(9) Kangzhou Wang, Lisheng Guo, Weizhe Gao, Baizhang Zhang, Heng Zhao, **Jiaming Liang**, Na Liu, Yingluo He, Peipei Zhang, Guohui Yang, Noritatsu Tsubaki. One-Pot hydrothermal synthesis of multifunctional ZnZrTUD-1 catalysts for highly efficient direct synthesis of butadiene from ethanol. *ACS Sustainable Chemistry & Engineering*. **9**, 10569–10578 (2021).

(10) Fei Chen, **Jiaming Liang**, Fan Wang, Xiaoyu Guo, Weizhe Gao, Yasuharu Kugue, Yingluo He, Guohui Yang, Prasert Reubroycharoen, Tharapong Vitidsant, Noritatsu Tsubaki. Improved catalytic

activity and stability of Cu/ZnO catalyst by boron oxide modification for low-temperature methanol synthesis. *Chemical Engineering Journal*. **458**, 141401 (2023).

(11) Lijun Zhang, Weizhe Gao, Fan Wang, Chengwei Wang, **Jiaming Liang**, Xiaoyu Guo, Yingluo He, Guohui Yang, Noritatsu Tsubaki. Highly selective synthesis of light aromatics from CO_2 by chromium-doped ZrO_2 aerogels in tandem with HZSM-5@SiO_2 catalyst. *Applied Catalysis B: Environmental*. **328**, 122535 (2023).

(12) Fei Chen, **Jiaming Liang**, Fan Wang, Weizhe Gao, Yasuharu Kugue, Yingluo He, Xiaoyu Guo, Guohui Yang, Guangbo Liu, Jinhu Wu, Prasert Reubroycharoen, Tharapong Vitidsant, Noritatsu Tsubaki. Alcohol solvent assisted synthesis of metallic and metal oxide catalysts: as-prepared Cu/ZnO/Al_2O_3 catalysts for low-temperature methanol synthesis with an ultrahigh yield. *ACS Catalysis*. **13**, 6169–6184 (2023).

(13) Lisheng Guo, Peipei Ai, Xinhua Gao, Hao Wu, Xianbiao Wang, Yasuharu Kugue, **Jiaming Liang**, Weizhe Gao, Xiaoyu Guo, Jian Sun, Song Sun, Noritatsu Tsubaki. Microwave-assisted carbon-confined iron nanoparticles for steering CO_2 hydrogenation to heavy hydrocarbons. *EES Catalysis*. **1**, 516–528 (2023).

(14) Wenhang Wang, Ruosong He, Yang Wang, Meng Li, Jianxin Liu, **Jiaming Liang**, Shuhei Yasuda, Qiang Liu, Mingbo Wu, Noritatsu Tsubaki. Boosting methanol-mediated CO_2 hydrogenation into aromatics by synergistically tailoring oxygen vacancy and acid site properties of multifunctional catalyst. *Chemistry-A European Journal*. **40**, e202301135 (2023).

List of conferences

(1) **Jiaming Liang**, Lisheng Guo, Noritatsu Tsubaki. Direct conversion of CO_2 to aromatics over K-Zn-Fe/ZSM-5 catalysts via a Fischer-Tropsch synthesis pathway. *2021 International Chemical Congress of Pacific Basin Societies,* **2021**, Honululu, America. (Poster)

(2) **Jiaming Liang**, Lisheng Guo, Noritatsu Tsubaki. Direct conversion of CO_2 to aromatics over K-Zn-Fe/ZSM-5 catalysts via a Fischer-Tropsch synthesis pathway. *The 19th Korea-Japan Symposium on Catalysis,* **2023**, Seoul, Korea. (Poster)

(3) **Jiaming Liang**, Lisheng Guo, Noritatsu Tsubaki. Direct conversion of CO_2 to aromatics over K-Zn-Fe/ZSM-5 catalysts via a Fischer-Tropsch synthesis pathway. *The 9th Tokyo conference on advanced catalytic science and technology (TOCAT9),* **2022**, Fukuoka, Japan. (Poster)

Acknowledgments

First of all, I would like to express my sincere thanks to my supervisor, Professor Noritatsu Tsubaki, for his hard work and help in the process of establishing the thesis, the experimental process, and the final paper. With his rigorous academic attitude, generous and kind-hearted mind, and positive and optimistic attitude towards life, my teacher has set an example for my lifelong learning. His teaching and encouragement will encourage me to make great efforts and pioneer innovation on the road of research and teaching.

At the same time, I would like to express my heartfelt thanks to Associate Professor Guohui Yang for his help and valuable guidance in my study. His erudition about science not only inspired my study during the Ph.D. but also inspired my future study and life.

I am very grateful to all the Chinese and Japanese students in our laboratory who help me in many ways and provide a very enjoyable atmosphere for me during the research period. They helped me a lot in both research and life.

Furthermore, I want to thank my family and two lovely kittens, Yomi and Chomi, who provided meticulous care and company during the five years I lived in Japan.

Special thanks belong to my parents, especially my father, who provided me with a lot of support in my research career.